CALIBRATION AND FLIGHT OF A BALLOON-BORNE O_2 ATMOSPHERIC BAND FABRY-PEROT SPECTROMETER

MICHAEL VOUTSOGIANNAKIS

A THESIS SUBMITTED TO THE FACULTY OF GRADUATE STUDIES

IN PARTIAL FULFILLMENT OF THE REQUIREMENTS FOR THE

DEGREE OF

MASTER OF SCIENCE

GRADUATE PROGRAM IN PHYSICS AND ASTRONOMY

YORK UNIVERSITY

TORONTO, ONTARIO

AUGUST 2017

Abstract

The Fabry-Perot spectrometer is an extremely useful tool for retrieving spectral information of the Oxygen A-band at nadir viewing angles, as well as for remote sensing purposes. Testing the performance of this spectrometer will help us determine possible limitations and improvements needed to be carried out for future missions, so that the scientific objectives can be met successfully. For the calibration setup, a narrow line argon source was used and the procedure was carried out by varying the gap spacing between the etalon plates, thus performing step scans that cover the entire free spectral range. Valuable information can be acquired, such as the reflective Finesse of the etalon, the degree of parallelism and flatness of the plates, as well as the temperature coefficient of the etalon. Measurements were also performed on O_2 interference filters, making use of a diffraction grating spectrometer, in order to understand their behavior with temperature change.

Acknowledgments

I would like to acknowledge my supervisor, Dr. Jinjun Shan, professor of space engineering at York university, who offered invaluable advice and guided me throughout my graduate studies. He was responsible for the success of this project as well as the cooperation among the research team involved.

Key team members that contributed significantly to the development of this research project were Prof. Gordon Shepherd and Dr. Chris Sioris. Gordon Shepherd, professor emeritus in the department of Earth and Space science at York University, offered valuable advice regarding lab calibration measurements, as well as data analysis regarding the Fabry- Perot. Dr Chris Sioris, attended the balloon campaign in Kiruna and mainly focused on spectral analysis and acquisition of data during the flight observations. Brian Solheim carried out the work done on the front-optics tube and assisted me

in the optical assembly and the lab setup used for the calibration procedure. Lastly, Dr. Yuan Ren was in charge of the electrical and mechanical components, that were critical for the correct operation of the spectrometer.

Last, but certainly not least, I would like to acknowledge the Canadian Space Agency (CSA) for financial support and MPB Communications Inc. for technical support during this project.

Contents

Abstract ii

Acknowledgments iii

Table of Contents v

List of Tables vii

List of Figures viii

1 Introduction 1

1.1 Scientific objectives and motivation 1

1.2 Thesis Outline 5

2 Fundamentals of a Fabry-Perot Spectrometer 8

2.1 The theory behind Fabry-Perot interferometers 8

2.2 Scanning the Fabry-Perot spectrometer 14
2.3 Imperfections associated with the design and performance of the Fabry-Perot 18

3 Tests before Kiruna flight campaign **21**
3.1 Finding the correct type of lens 21
3.2 Optical setup 24
3.3 Spatially scanning the Fabry-Perot 28
3.4 Determine the variation of the finesse across the etalon 34
3.5 Determine the initial spacing between the plates and the order of interference for the centre fringe 37
3.6 Optimal piezo readouts for improved parallelism 40

4 Re-calibration of the Fabry-Perot spectrometer **47**
4.1 Modelling of the O_2 filters used during the flight 47
4.2 Testing the temperature dependence of the Fabry-Perot 53
4.2.1 Using a thermocouple 53
4.2.2 Using a temperature controller 56
4.3 Calculate the linear dispersion of the diffraction grating 58
4.4 Determine the temperature dependence of the filters 63

4.5 Determining the O_2 filter passband 69

4.6 Spectrometer wavelength calibration 77

4.7 Creating a 2-D map representing the change in gap spacing . . 79

4.8 Calibration and responsivity calculation of the flight instrument 82

4.9 Characterization of the improved Fabry-Perot 88

5 Atmospheric observations during Alice Springs flight campaign 92

5.1 Recovering the true spectrum for the O_2 band from the observed spectrum 92

5.2 Variation of albedo during flight 104

6 Conclusions and future work 110

Bibliography 115

List of Tables

3.1 FWHM, FSR and Finesse calculated for different fitting curves 33

4.1 Parameters for Filter 1, as were supplied by Andover 49

4.2 Parameters for Filter 2 49

List of Figures

1.1 (a)The enclosure that houses the F-P spectrometer along with all the instrumentation is contained in a special gondola. The F-P is on the left with a 45-degree mirror bearing the label SDCNLab allowing the instrument to look vertically downwards. (b)Side view of the gondola used in Kiruna, Sweden. The sealed tube enclosing the F-P is oriented vertically, facing the ground. 4

2.1 Illustration of the transmitted field amplitude. 9

2.2 The Airy function of a Fabry-Perot for different reflectances (R=0.1-0.91). 10

2.3 Schematic of the reflected and transmitted amplitudes in the F-P 11

2.4 (a)Schematic of the multiple interference pattern produced in the etalon of a gap width of d and a refractive index of n when the angle of incidence is θ. A, R and T refer to the mirror absorption, reflectance and transmittance respectively and the ϕ is the phase that is introduced after reflection [8]. (b)Drawing that illustrates the basic operation of a Fabry-Perot spectrometer [9]. 12

2.5 The transmittance profile of the spectrometer and important factors associated with it's performance [11]. 13

2.6 Etendue parameter of an interferometer (in our case the Fabry-Perot) [13]. 17

2.7 (a)Categories of plate defects. (b)Variation of defect, reflective and effective Finesse as a function of reflectivity. 20

3.1 a)The Absolute quantum efficiency curve for different wavelengths at 25 °C, as provided by the sensor manufacturer. b)Apogee Alta F6 CCD camera 25

3.2 (a)Opteka lens attached to the CCD camera with an adaptor. (b)Rear view of Opteka telephoto lens. 26

3.3 (a)F-P without the enclosure showing the clear aperture and the position of the piezos. (b)The enclosure of the Fabry-Perot. Credits: MPB Communications Inc. 27

3.4 The transmission curve of the Argon interference filter, as was supplied by the manufacturer 28

3.5 Airy function versus piezo displacement, relative and physical gap spacing, as well as wavelength. 29

3.6 Comparison of the FWHM as measured for both passbands for three different fits: a Gaussian, an Airy and a Lorentzian fit 32

3.7 Fringes generated from the F-P 33

3.8 Setup with aperture in front of F-P 35

3.9 Setup with aperture in front of F-P 36

3.10 The centre fringe is concentrated in a small bright area and the second ring is only visible from the corners of the detector 38

3.11 The contour of the rings when the aperture was positioned at the left and right of the F-P. The images are very similar and the correlation is the largest (0.6657). 41

3.12 The contour of the rings when the aperture was positioned at the left and right of the F-P. The images are very different and the correlation is the lowest (-0.3729). 41
3.13 The contour map of the 2-D correlation coefficient 42
3.14 Lowest correlation achieved (-0.0179) when the aperture was positioned up and down 43
3.15 Highest correlation achieved (0.6925) when the aperture was positioned up and down 43
3.16 The interference fringes that were produced by the F-P for five different positions (10 mm from the etalon centre) of the aperture (up, down, left, right, center). The sensor readouts are 380, 404 and 653 nm for each piezo respectively (The relative displacement is 80 nm). 45
3.17 The interference fringes when the readouts are 680, 704 and 953 nm. 46

4.1 Filter 1 simulated passbands 51
4.2 Filter 2 simulated passbands 52
4.3 Transmittance versus wavelength as a function of temperature 55
4.4 Change in wavelength with temperature 55

4.5 Transmittance versus wavelength 57
4.6 Change in wavelength with temperature 57
4.7 Optical layout of a Czerny-Turner monochromator. M_1 and M_2 are the mirrors and G represents the grating. 59
4.8 Change in position of the spectral line as the grating rotates. . 61
4.9 Diffraction grating spectra versus pixel number for different wavelengths 62
4.10 Shift in peak position versus wavelength change 62
4.11 Top view of setup showing the optical tube and the Tungsten source 63
4.12 Transmittance versus pixel number 65
4.13 Gaussian fit for each step scan 65
4.14 Peak shift versus temperature change 66
4.15 Angle of rotation of diffraction grating versus incident wavelength 68
4.16 Observed spectra of filter for different entrance slit widths (0.07-0.4 mm) 70
4.17 Transmission curve for the filters, generated from an inverse transformation 76

4.18 Change in position of the spectra as the grating rotates. . . . 77

4.19 True wavelength versus wavelength from spectrometer reading 78

4.20 Optical setup to generate a gap spacing map 80

4.21 2-D contour of etalon 81

4.22 2-D gap spacing map, 500 x 400 pixel area 81

4.23 (a)Certificate for the 1-kW tungsten lamp showing the calibrated values of irradiance for a wavelength range from 3000 Åto 12000 Å. (b)Calibrated reflectance factors for the same wavelength range 83

4.24 The calibrated irradiance values along with the fit provided by Saunders 85

4.25 (a)Step scan within a wavelength range of (761.35-762.5 nm). (b)Second-order peak curve representing the transmittance in the spectral range 761.7-762.2 nm. 87

4.26 Improved step scans for angles of incidence 0-0.98 degrees . . . 89

4.27 Mask designed for the F-P by MPB Technologies Inc. 90

5.1 Change in temperature for the entire duration of the balloon flight. 93

5.2 The observed spectrum generated in Alice Springs from step scan 36. 95

5.3 Simulated spectrum of the O_2 absorption band. Courtesy of Dr. Chris Sioris. 96

5.4 Shift of filter wavelength with temperature change (δT=6.62^{o}C) during flight. 98

5.5 Instrumental passband (Airy profile) retrieved at 24.5°C and at 29.82°C respectively. 100

5.6 The observed spectrum generated in Alice Springs from step scan 36 at θ=0.523 degrees and corrected for temperature change 101

5.7 The true spectrum generated from the recorded and filter profiles 102

5.8 O_2 atmospheric spectrum, filter and observed profile. 103

5.9 Change in maximum observed radiance with time and scan number 105

5.10 Radially averaged step scans 15-50 106

5.11 Solar zenith angle as a function of time (Alice Springs local time) 107

5.12 Variation in observed radiance as a function of scan number. Courtesy of Dr. Chris Sioris. 108

5.13 Change of albedo as a function of scan number, after the removal of the solar zenith angle dependence. 109

Chapter 1

Introduction

1.1 Scientific objectives and motivation

The Oxygen A-band refers to the part of the atmospheric spectum that extends from 759 nm to 770 nm. It represents an important feature in the near-infrared band of the spectrum, and has been studied for remote sensing purposes from ground based instruments as well as satellites. The O_2 is usually preferred over the $^1\Delta$ band of O_2, which emits at 1.27 μm, which is close to the peak emission of CO_2 at 1.6μm. However, the A O_2 band is significantly affected more by airglow at higher altitudes and thus gives out higher radiance at these shorter wavelengths.

The principal scientific goal of this project is the study of the molecular Oxygen $^{16}O_2$ emission line (P1) at a wavelength of 762.3 nm. Since all Oxygen A-band absorption line parameters are dependent on pressure, photon path length distributions andvertical information regarding aerosols and clouds can easiily be obtained [1]. Also, since 20.9% of the air is composed of molecular Oxygen O_2, the vertical column density (VCD) can easily be mapped in units of (molecules/cm^2). O_2 can be combined with measurements of Carbon Dioxide VCD to give a CO_2 column-averaged volume mixing ratio (known as xCO_2). One main reason to measure CO_2 volume mixing ratio rather than CO_2 VCD is that the latter is much influenced by surface elevation (i.e. smaller columns over mountains).

Apart from the determination of VCD, other parameters can be retrieved, such as surface albedo, from the continuum spectrum as well as the surface pressure, from the edges of the absorption line. Information regarding aerosols can be obtained from the core of this line. Aerosols are important for air quality and climate, as they interact with the Earth's radiation budget by changing the amount of shortwave radiation leaving the Earth's surface. They have also been associated with adverse health effects as fine aerosols can enter deeply into the lungs leading to respiratory and cardiovascular health

outcomes for humans [2].

The retrieval of properties associated with cloud and aerosol can be done with high-resolution A-band spectra that can discriminate atmopsheric scattering from surface scattering [1]. For this purpose, the Fabry-Perot spectrometer offers some advantages over other instruments such as diffraction gratings and Fourier transform spectrometers. This is due to the fact that the Fabry-Perot can achieve a high resolution resulting in peaks of radiation amongst almost zero transmission and can be made very small and compact without degrading the resolving power.

The light-weight (1.2 kg) miniature high resolution spectrometer used to obtain the measurements mentioned above was developed by MPB Communications Inc. (MPBc) and allows for a wide spectral range to be covered in the atmosphere, as a result of fine wavelength tuning. The F-P was integrated into a payload that consisted of fore-optics elements, interference filters, a telephoto lens, a CCD camera, as well as various electronic and thermal components, such as amplifiers, microcontrollers and heat sensors. The entire optical assembly was enclosed into a sealed tube and was successfully launched on a stratospheric balloon from Esrange Space Center in Kiruna, Sweden, on September 3 2016. The second balloon campaign to

re-launch an improved version of the F-P spectrometer took place in Alice Springs, Australia, on April 9, 2017.

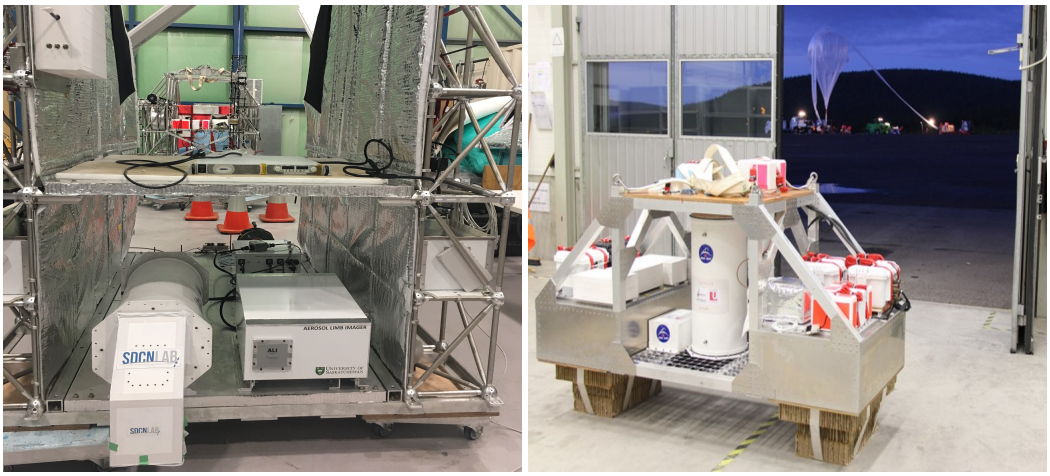

(a) (b)

Fig. 1.1: (a)The enclosure that houses the F-P spectrometer along with all the instrumentation is contained in a special gondola. The F-P is on the left with a 45-degree mirror bearing the label SDCNLab allowing the instrument to look vertically downwards. (b)Side view of the gondola used in Kiruna, Sweden. The sealed tube enclosing the F-P is oriented vertically, facing the ground.

1.2 Thesis Outline

Below, the basic structure of the thesis is outlined:

- Chapter 2

  The basic theoretical concepts are introduced in this chapter regarding the Fabry-Perot spectrometer, important equations, methods of wavelength scanning and any imperfections that are associated with it's operation.

- Chapter 3

  In this chapter lab tests that were performed before the first balloon campaign in Kiruna are described in detail. The chapter begins with describing the procedure that was carried out in order to determine the correct lens for the experimental setup, which is described afterwards. Then, the chapter proceeds to the way a step scan is performed and important parameters that were retrieved such as the reflective Finesse, the Full Width at Half Maximum (FWHM), the initial etalon spacing and the interference order of the F-P. The last section refers to the optimal readouts of the piezos that were required for best parallelism between the plate mirrors of the F-P.

- Chapter 4

  Chapter 4 focuses on tests that were done preceding the successful flight mission in Alice Springs. A modification of the F-P to improve it's Finesse was also implemented. The primary goal of these tests was to determine the temperature sensitivity for both the Fabry-Perot and the interference filters used during the flight. An attempt to generate a 2-D map was done, representing the variation of Finesse across the surface of the etalon. In addition to this, the filter passband was retrieved, using a different setup, that mainly involved a diffraction grating spectrometer. Finally, a calibration procedure is described that was done with a Tungsten lamp to calculate the responsivity of the instrument (Fabry-Perot).

- Chapter 5

  Here, the chapter describes in detail the data analysis that was done using the data that were retrieved after the balloon campaign in Alice Springs.

- Chapter 6

  The conclusions that were obtained from the work done are outlined

here, regarding the instrument calibration and temperature tests conducted on the F-P. A brief summary and future work that needs to be carried out is mentioned in order to minimize errors related to filter measurements and improve data that was obtained from the flight.

Chapter 2

Fundamentals of a Fabry-Perot Spectrometer

2.1 The theory behind Fabry-Perot interferometers

The Fabry-Perot interferometer, in it's basic form, consists of two flat and partially transmitting mirrors that usually have a very high value of reflectance (R=0.8-0.9). These mirror plates are separated by a distance d and are parallel to each other and the medium within the optical gap has a refractive index n. The transmittance spectrum is best described by the

Airy function [3]:

$$I = \frac{1}{1 + F\sin^2(\delta/2)} \tag{2.1}$$

where F is the coefficient of Finesse, $\delta = \frac{2\pi}{\lambda} 2nd\cos\theta$ is the phase difference between consecutive beams and I is the the ratio $\frac{I_t}{I_i}$ of the transmitted flux density I_t to the flux density of the incident wavefront I_i. This equalized intensity profile is the result of N exponentially decaying fields that are transmitted through an etalon contributing to a total amplitude that is given by [4]:

$$E_t = E_o[t^2 e^{i\delta} + r^2 t^2 e^{3i\delta} + r^4 t^2 e^{5i\delta} + ..] = E_o \frac{T e^{i\delta}}{1 - R e^{2i\delta}} \tag{2.2}$$

where T=$|t|^2$and R=$|r|^2$ are the transmission and reflection coefficients respectively and E_t and E_o the transmitted and incident field amplitudes that pass through the cavity. The airy function described in Eq.(2.1) is the ratio $\frac{I_t}{I_i} = \left|\frac{E_t}{E_o}\right|^2$=I. A schematic of the field amplitudes is shown below [4]:

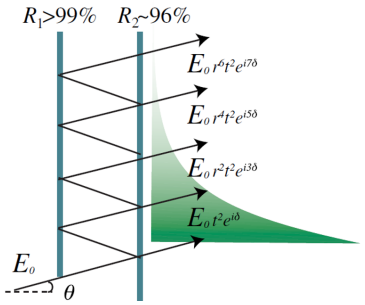

Fig. 2.1: Illustration of the transmitted field amplitude.

We can visualize the behavior of the Airy function in the following figure [5]:

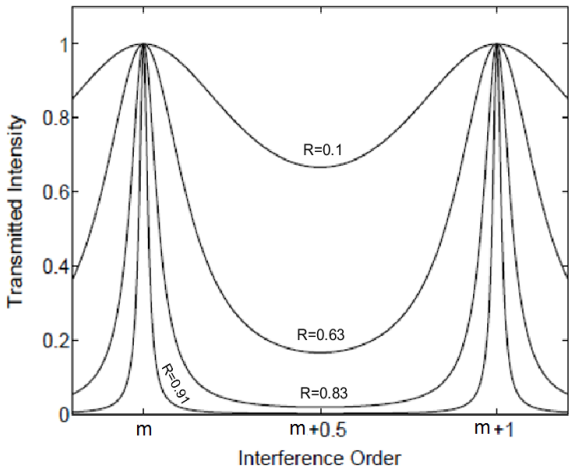

Fig. 2.2: The Airy function of a Fabry-Perot for different reflectances (R=0.1-0.91).

In Fig. 2.2 the transmitted flux-density distribution is plotted against the interference order m, or otherwise, versus the phase difference δ. The phase can be defined in terms of optical path difference $t = 2nd\cos\theta$ for a refractive material or otherwise $t = 2d\cos\theta$, if we have a parallel air plate. This is the path difference between successive beams incident at an angle θ through the air-gapped etalon with a plate spacing d, as is illustrated below

in Fig. 2.3 [6]:

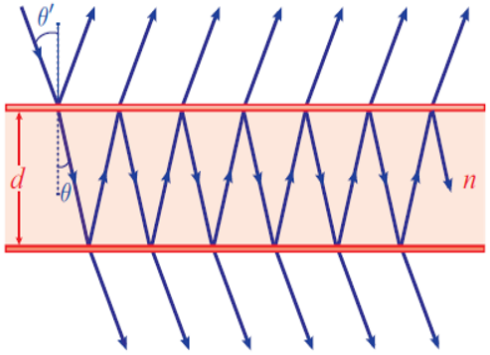

Fig. 2.3: Schematic of the reflected and transmitted amplitudes in the F-P

Therefore each beam experiences a lag in phase by an amount of $\delta = 2\pi \mathrm{kt} = \frac{2\pi}{\lambda} 2nd\cos\theta$, where $\mathrm{k} = \frac{1}{\lambda}$ is the wavenumber (cm^{-1}), which is defined as the number of waves in a cm [7]. The function reaches a maximum value when $\delta = 2\mathrm{m}\pi$ and constructive interference occurs. The Airy function is equal to unity in this case regardless of the coefficient of Finesse (F). Once the reflectivity of the mirrors increases, F also increases in value and the width of the peaks, as well as the transmitted intensity in between the maxima decrease. The expected result is that as reflectivity approaches unity, the Fabry-Perot acts as an optical resonator, letting in only selected frequencies, as a result of the narrowing of the peaks.

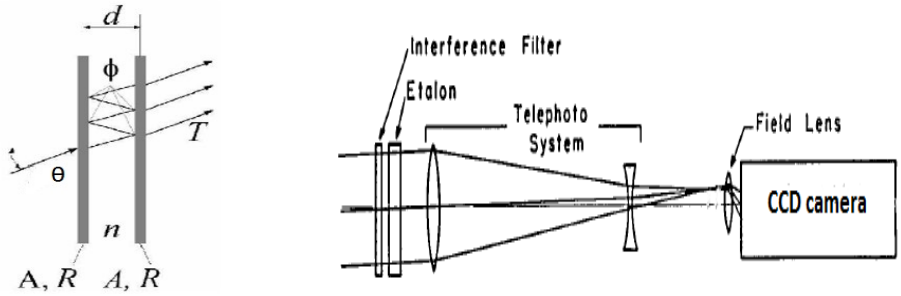

(a) (b)

Fig. 2.4: (a)Schematic of the multiple interference pattern produced in the etalon of a gap width of d and a refractive index of n when the angle of incidence is θ. A, R and T refer to the mirror absorption, reflectance and transmittance respectively and the ϕ is the phase that is introduced after reflection [8]. (b)Drawing that illustrates the basic operation of a Fabry-Perot spectrometer [9].

We can define the separation between consecutive orders, in units of wavelength as the Free Spectral Range or FSR [10]:

$$FSR = \frac{\lambda^2}{2nd} \tag{2.3}$$

where λ is the wavelength of the light incident on the cavity and d the mirror spacing. The full width of the Airy curve when the irradiance reaches half it's maximum value is called the Full Width at Half Maximum (FWHM),

given by [10]:

$$FWHM = \frac{\lambda(1-R)}{n\pi\sqrt{R}} \tag{2.4}$$

An important factor which defines the performance of the spectrometer and is directly related to the above quantities is the Finesse, as introduced earlier in Eq. (2.1), which can be written as [10]:

$$Finesse = \frac{FSR}{FWHM} = \frac{\pi\sqrt{R}}{(1-R)} \tag{2.5}$$

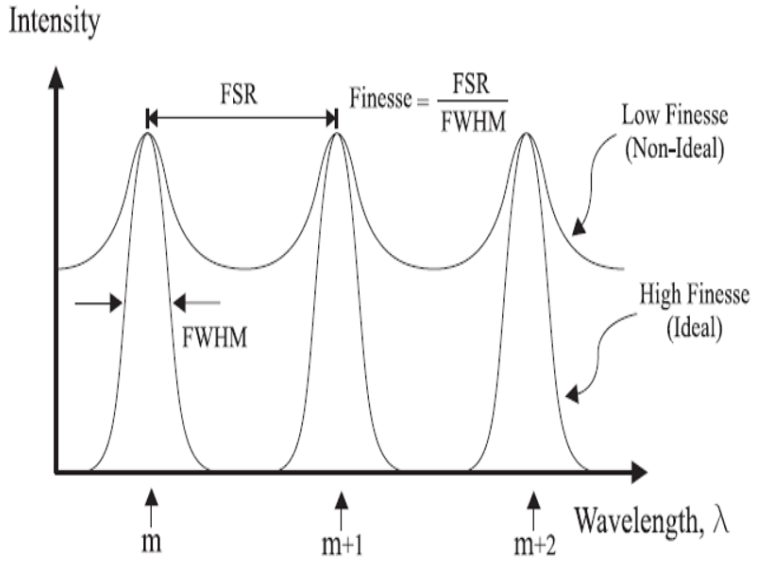

Fig. 2.5: The transmittance profile of the spectrometer and important factors associated with it's performance [11].

From Fig. 2.5 it is clear that a higher Finesse results in sharper trans-

mission peaks and narrower bandwidths, thus increasing the spectral resolution of the spectrometer. The dependence of the Finesse described above relies only on the reflectivity of the two mirror plates of the F-P cavity, so it is better defined as the reflectivity Finesse F_R. As was mentioned previously, when the phase reaches a value of δ=2mπ the transmission reaches a maximum and this occurs when:

$$2nt\cos\theta = m\lambda \tag{2.6}$$

The above equation can be satisfied by varying one of the parameters n, θ, m and t in order to change λ, that is, to create a spectral scan.

2.2 Scanning the Fabry-Perot spectrometer

Scanning of the spectrometer usually involves varying the position where the passband peak occurs λ and this can be achieved by varying the other parameters in Eq. 1.5. The variables that can be altered are n, d and θ keeping the order m fixed. These three ways are described below :

- Scanning by varying the distance between the spectrometer plates

  In this method, which is used for the experimental tests throughout the thesis, the gap spacing is varied and this is usually done mechan-

ically, the most common ways being magnetostriction and the use of piezoelectric actuators. If eq. 1.5 is differentiated we get [12]:

$$\frac{d\lambda}{dt} = \frac{\lambda}{t} = \frac{2n}{\lambda} FSR \tag{2.7}$$

It is clear from the above that in order to cover one full FSR (Free Spectral Range), a displacement of $\lambda/2$ is needed, in etalon spacing. For this reason, this method is more common for low resolution spectroscopic applications, as the FSR is relatively large.

- Refractive index scanning

  Here, the refractive index of the medium (n) within the etalon cavity is changed with time. This can be accomplished by varying the pressure (P) of the gas medium in the F-P, assuming a linear relationship between n and P (n-1)/P=α [12] , known as the Gladstone-Dale law where α is a constant. Differentiating as before, for a given pressure change dP one gets [11]:

$$\frac{d\lambda}{dP} = \frac{\alpha}{n\lambda} \tag{2.8}$$

  Since the scanning range is independent of the FSR, a change in gap spacing t will not affect the result. Thus, the wavelength extends over a range of a few Angstroms, which is useful for high-resolution studies

that employ a limited scanning range.

- Spatial scanning

  The third technique involves varying the angle of the radiation through the etalon in order to scan a wavelength range. If λ and λ_o are the wavelengths that pass through at θ>0 and at normal incidence respectively one can get the following equation [9]:

$$\lambda - \lambda_o = -\lambda_o \frac{i^2}{2n^2} \tag{2.9}$$

  where i is the angle between the incoming rays of light and the etalon normal and n the refractive index. The advantage of this technique lies on the fact that, as with refractive index scanning, the scanning range is independent of the spacing t. This permits the use of an etalon with a fixed spacing as well as a solid medium. By differentiating Eq. (2.9) we get the following relationship between the spectral (dλ) and angular (di) width [9]:

$$d\lambda = -\frac{\lambda_o i di}{n^2} \tag{2.10}$$

  From Eq. (2.10) it is clear that the use of a solid etalon results in an aperture with an angular width (area) larger by a factor of n^2 compared

to that of an air-spaced etalon. Therefore, the optical throughput of the system, which is usually given in terms of *Etendue*, will be larger. Etendue is an important parameter that helps us describe the light collecting efficiency of an interferometric system, as well as an optical assembly. It can be thought of as the light-gathering power and can be defined as the product of the area of the entrance aperture by the solid angle limited by the spectral width mentioned before (di) [13]. To better understand the concept of this parameter a figure is provided below:

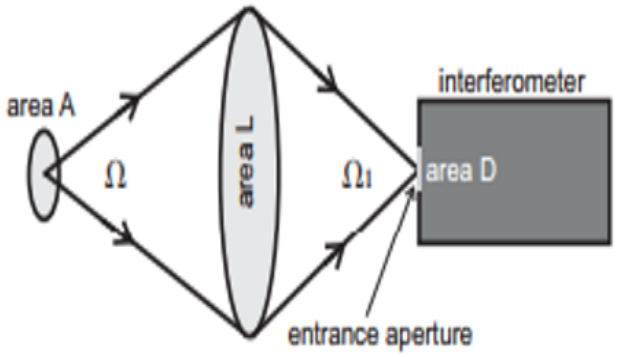

Fig. 2.6: Etendue parameter of an interferometer (in our case the Fabry-Perot) [13].

In Fig. 2.6 the source (area A), the collecting lens (area L) and the

solid angles (Ω, Ω_1) are shown. The etendue is given by

$$E = A * \Omega \tag{2.11}$$

2.3 Imperfections associated with the design and performance of the Fabry-Perot

In the previous sections, it was assumed that we were dealing with a perfect etalon, where the reflectivity finesse (F_r) is only dependent on the reflectivity of the plates of the F-P, assuming that they both reflect exactly the same way. However, in real situations, the etalon is far from ideal and mirror defects play an important role in limiting practical values of reflectivity. These defects result in a wider bandwidth and a reduced Finesse for a non-ideal F-P spectrometer. The imperfections are outlined below:

- **Spherical deviation**

  The degree of the etalon flatness can be expressed by the fraction of wavelength $\delta_s = \lambda/\alpha$. This corresponds to the difference in thickness between the center of the etalon and its edge. In the case where the mirror surfaces deviate from ideal flat planes, the beams do not reflect back precisely and the gap spacing is changed, consequently, there is

a noticeable divergence from the ideal path. Therefore, this changes the phase relationship between the waves and results in wider peak transmission curves [14]. The defect Finesse that arises from departure from flatness is given by [10]:

$$F_s = \frac{\lambda}{2\delta_s} \tag{2.12}$$

where δ_s is the spherical deviation.

- **Surface irregularities**

  Another important factor that might affect the performance of the spectrometer is the roughness that the plates might exhibit. A Gaussian distribution is assumed for the surface roughness and the defect Finesse can be written [10]:

$$F_{rms} = \frac{\lambda}{4.7\delta_{rms}} \tag{2.13}$$

  where δ_{rms} is the root-mean-square deviation following a Gaussian distribution.

Also, the finite size of the etalon is another characteristic that might have an effect on the overall performance of the system. This is more noticeable at large off-axis angles, with high reflectances and high resolutions where the reflected beams pass over the edge of the surface of the mirror plates re-

ducing the responsivity of the instrument. Having specified the spherical and rms Finesse (F_s,F_{rms}), the defect Finesse which results from the combination of both can be written [10]:

$$F_D = \left[\frac{1}{F_s^2} + \frac{1}{F_{rms}^2}\right]^{-1/2} = \frac{\lambda}{(4\delta_s^2 + 22\delta_{rms}^2)^{1/2}} \tag{2.14}$$

Knowing now the defect Finesse (F_D) and the reflective Finesse (F_R) the total Finesse of the etalon which is termed the effective Finesse can be deduced from :

$$\frac{1}{F_E^2} = \frac{1}{F_R^2} + \frac{1}{F_D^2} \tag{2.15}$$

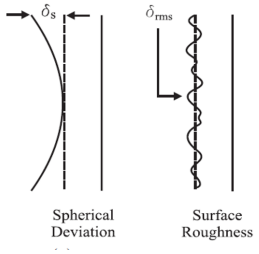

(a)

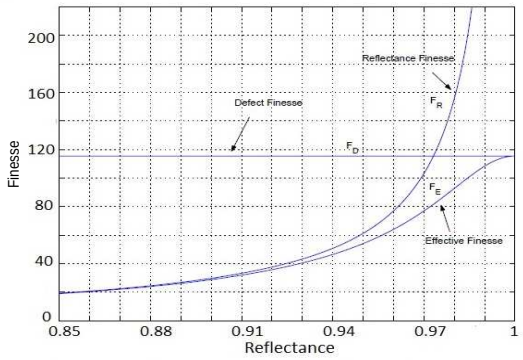

(b)

Fig. 2.7: (a)Categories of plate defects. (b)Variation of defect, reflective and effective Finesse as a function of reflectivity.

Chapter 3

Tests before Kiruna flight campaign

3.1 Finding the correct type of lens

The correct type of lens that should be chosen for our purposes will be specified by two parameters: the focal length and the F-number. Assuming that the medium between the reflecting plates of the Fabry-Perot etalon is air, the refractive index of the medium will be n≈1. The light rays travel from air through the etalon plate, continuing through the air-spaced etalon and then through the second plate exiting into air. The angle that is needed

in order to achieve spatial scanning is given from rearranging E.q. (2.9) and we get:

$$i = n\sqrt{\frac{2(\lambda_o - \lambda)}{\lambda_o}} \tag{3.1}$$

where λ_o-λ is the half-width of the spectral line we want to observe at λ_o=762.31 nm, i is the range of angles (in radians) involved in the spatial scan and n the refractive index of the medium within the etalon. The spectral range in the O_2 atmospheric spectrum that is intended to be covered is ≈0.32 nm, as was given by Dr. Chris Sioris. Half of this range is equal to λ_o-λ=0.16 nm and this value represents the change in wavelength as we go from the centre of the image (our detector, i=0 degrees) to the edges of the CCD, which corresponds to off-axis angles.

The bandwidth of the O_2 line is known to be around 0.23 nm, so the half width would be λ_o-λ=0.115 nm and because n≈1 we have i= 0.0174 radians or i=0.9975 degrees. This is essentially the angle that will scan the same wavelength range as a step scan is carried out, by moving the etalon plates. As the angle though the etalon is approximately the same as the angle outside the plates the numerical aperture is [15]:

$$NA = n\sin i \approx \sin i \tag{3.2}$$

So NA=sin(0.9975)=0.0174. The numerical aperture can be described as

the light gathering capability of an objective lens or optical element and is directly proportional to the radiant flux through the aperture. The angle i can otherwise be described as the half cone of illumination.

The clear aperture (CA) of the Fabry-Perot, as provided by MPB Technologies is given as CA=23 mm, so the f-number can be found from [16]:

$$f/\# = \frac{f}{CA} \tag{3.3}$$

where f is the focal length. Since the incident angle i on the Fabry-Perot defines a half cone of light with a diameter of CA=23 mm and a height of f the numerical aperture will become :

$$NA = \sin i = sin\left[arc\tan\left(\frac{CA}{2f}\right)\right] \approx \frac{CA}{2f} = \frac{1}{2(f/\#)} \tag{3.4}$$

Thus $f/\#=\frac{1}{2(NA)}$=28.73 and the focal length of the lens will be $f=(f/\#)$(CA)=660.92 mm. This is a relatively large value of focal length and because $\frac{f}{CA}\gg 1$, the required lens for our application would be a telephoto or a telecentric lens with an adjustable focal length in the range 300-800 mm. After searching for commercial lenses an Opteka telephoto lens was purchased, having a focal length range of 420-800 mm and an aperture range of $f/8.3$-16.

Since the Opteka lens will connect with a 1 MP Apogee F6 CCD

camera, it is important that the flange focal distance of the lens is examined and compared with the flange to focal plane distance of the camera. For this reason, the lens was mounted on a tripod so that it received light from a distant source (laser) that was available in the lab. Assuming the distant source is at infinity,a white screen was placed at the rear of the lens and was shifted it until a discrete image was produced. The distance from this screen to the back flange of the body of the lens is the flange focal depth and is estimated at FFD_{lens}=55 mm. The Apogee camera has a flange back distance of FFD_{camera}=26 mm, so a spacer of thickness $d_{adapter}$=FFD_{lens}-FFD_{camera}=29 mm will be needed.

3.2 Optical setup

The key components involved in the experimental setup used in order to mechanically scan the Fabry-Perot are the following:

- **A CCD camera**

  The camera that we use is an Apogee Alta F6 CCD camera, which has a high resolution 1.0 megapixel full frame sensor with dimensions 24.6 x 24.6 mm. The total number of effective pixels is 1024 x 1024

and each element of the array has a size of 24 x 24 μm. It features a 43 mm shutter, the back focal distance is 2.6 cm and the dark current reaches typical values of 0.110 e^-/pixel/sec. The quantum efficiency at wavelengths 400 nm and 560 nm is 40% and 72% respectively. As we can see from the QE curve below, the quantum efficiency for the spectral region of our interest (762-763 nm) will approximately reach 50%.

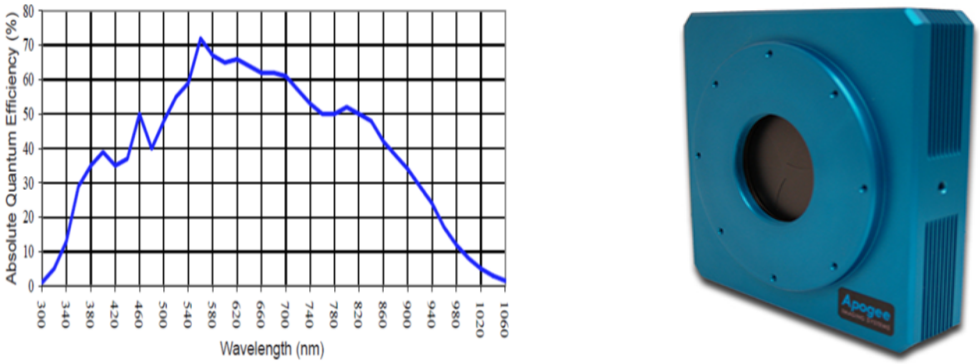

Fig. 3.1: a)The Absolute quantum efficiency curve for different wavelengths at 25 °C, as provided by the sensor manufacturer. b)Apogee Alta F6 CCD camera

- **A 420-800 mm telephoto lens**

  The Opteka telephoto lens, as was briefly described in section 3.1 features a focal length range of 420-800 mm with a manual focus as well

as an aperture (f-number) f/8.3-16. It has a 62 mm filter, a minimum focus distance of 1.6 m and a flange focal length 55 mm.

Fig. 3.2: (a)Opteka lens attached to the CCD camera with an adaptor. (b)Rear view of Opteka telephoto lens.

- **A Fabry-Perot spectrometer**

  The band-tuned spectrometer has a mass of 1.21 kg with the enclosure and a clear aperture of 23 mm. The enclosure has a diameter of 101.6 mm and a length of 76.2 mm. The distance between the plates is 0.555 mm and this value is varied by three piezos that are equally spaced in a circle with a 33 mm diameter. There is also a wedge of 0.167 degrees between the reflecting and non-reflecting surfaces of each flat. The purpose of this angle is to ensure that any weak reflection from the non-reflecting surfaces does not interfere with the Fringes produced

from the Fabry-Perot.

Fig. 3.3: (a)F-P without the enclosure showing the clear aperture and the position of the piezos. (b)The enclosure of the Fabry-Perot. Credits: MPB Communications Inc.

- **An interference filter**

  For the laboratory measurements, an Argon spectral lamp with a line at 738.2 nm was used. The line was isolated with a broadband interference filter that had a peak transmission of 51% at λ=739.38 nm. The bandwidth is 0.81 nm and the operating temperature is 25°C, as was provided by Andover.

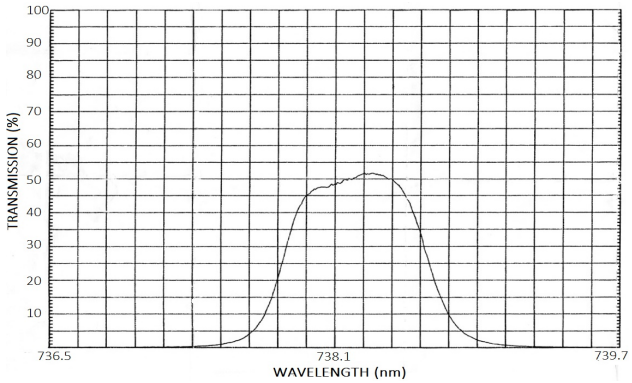

Fig. 3.4: The transmission curve of the Argon interference filter, as was supplied by the manufacturer

- A low intensity ORIEL 200W Argon light source

3.3 Spatially scanning the Fabry-Perot

A step scan was performed at an exposure time of 30 second, a step size of 19 nm and a range of 400-1000 nm. The transmittance (in units of arbitrary counts) is plotted against the reading of the piezos, the relative change in gap spacing, the nominal (physical) gap spacing, as well as the wavelength.

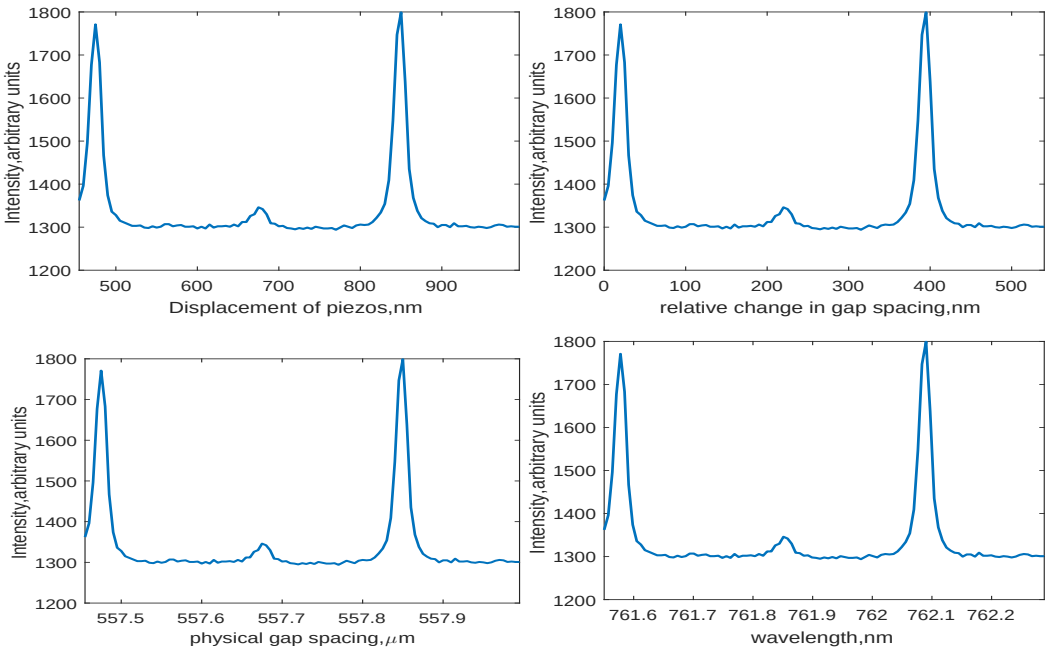

Fig. 3.5: Airy function versus piezo displacement, relative and physical gap spacing, as well as wavelength.

The above figures represent step scans that were carried out for one certain pixel on the CCD camera. In this case, the scans refer to the center pixel that has coordinates (512,512) in pixel units. The Finesse can be calculated from a step scan referring to the centre pixel (512,512), by estimating the Free Spectral Range and the FWHM of the spectral line. There are three ways to do this:

- Applying a Gaussian fit to the data. The function used is f_{Gauss}(x)=

$\alpha e^{\frac{-(x-b)^2}{(2c^2)}}$, where α is the peaks height which corresponds to the maximum transmittance,b is the position of the center of the peak (in wavelength units) and c the standard deviation. Applying Gaussian fits to both peaks and calculating these coefficients and taking the difference in the values of b the FSR is determined. This is essentially the distance from one peak to the next and is estimated at FSR=370 nm or FSR_{Gauss}=0.5 nm in gap spacing or wavelength units respectively. The FWHM is $\text{FWHM}_{Gauss}=2\sqrt{2\ln 2}c$=0.0237nm and the Finesse Finesse_{Gauss}=21.237.

- Applying a fit using an Airy function. The Airy function as described in the theoretical concepts is given by $f_{Airy}(\text{x})=\text{I}\frac{1}{1+fsin^2\delta/2}$, where $\text{f}=\frac{4R}{(1-R)^2}$ is the coefficient of Finesse and δ the phase shift. Solving for this coefficient the value for the coefficient of Finesse and therefore the Finesse will be $F=\frac{\pi\sqrt{f}}{2}$. We get f=316.48 and F=27.96 for the coefficient of Finesse and the actual value are calculated respectively and the FSR is estimated numerically by determining the peaks of the fitted curves and calculating the distance between them. Therefore, FSR_{Airy}=373.65 nm and the Finesse=27.96, so $FWHM_{Airy}=\frac{FSR_{Airy}}{Finesse_{Airy}}$=5.91

nm. In units of wavelength these parameters become FSR_{Airy}=0.506 nm and $FWHM_{Airy}$=0.0217 nm.

- Applying a Lorentzian fit to the data. A Lorenz function can be defined as f_{Lorenz}= I$\frac{(\Gamma/2)}{(\Gamma/2)^2+(x-b)^2}$, where I the maximum intensity, b the position of the peaks and Γ the FWHM of the Lorentzian curve. For this particular fit, the parameters are estimated at FSR$_{Lorenz}$=0.493 nm and FWHM$_{Lorenz}$=0.019 nm, a thus we get a Finesse of Finesse$_{Lorenz}$=25.94.

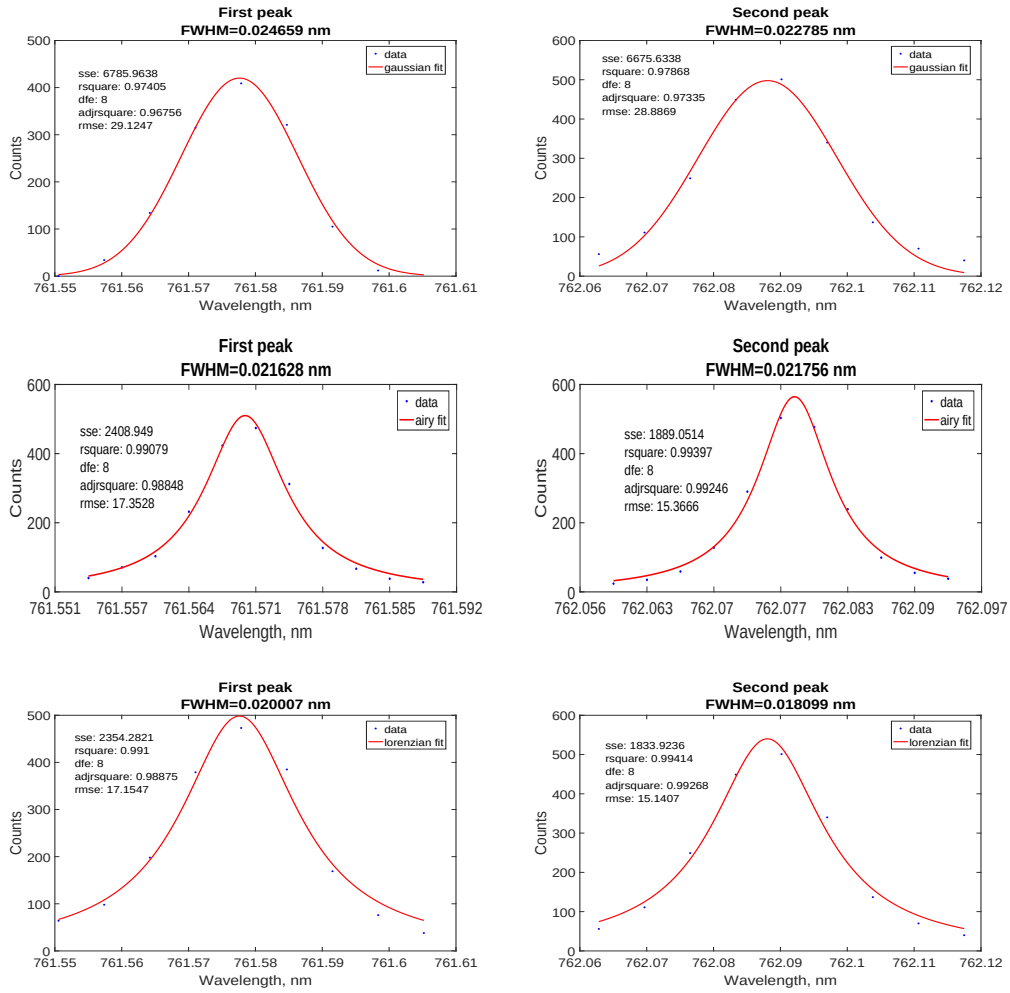

Fig. 3.6: Comparison of the FWHM as measured for both passbands for three different fits: a Gaussian, an Airy and a Lorentzian fit

From the subfigures above it is noticeable that the Lorentzian and the Airy fit yield better results than the Gaussian function. The correlation coefficient is $R_{first} \approx 0.991$ and $R_{second} \approx 0.994$ for the first and second peak

of the step scan respectively. The difference in the FWHM of the peaks for both methods of fitting is δ_{airy}=0.00013 nm and δ_{lorenz}=0.0019 nm. The small difference in bandwidths might be due to the plates of the F-P not being exactly parallel to one another.

Table 3.1: FWHM, FSR and Finesse calculated for different fitting curves

Fitting function	FWHM (nm)	FSR (nm)	Finesse
Gauss	0.0237	0.5	21.237
Airy	0.0217	0.506	27.96
Lorenz	0.019	0.493	25.94

The fringes that were produced on the CCD camera by the Fabry-Perot for different values of gap spacing are shown below. The relative change in the plate spacing as well as the change in wavelength is shown for each subfigure:

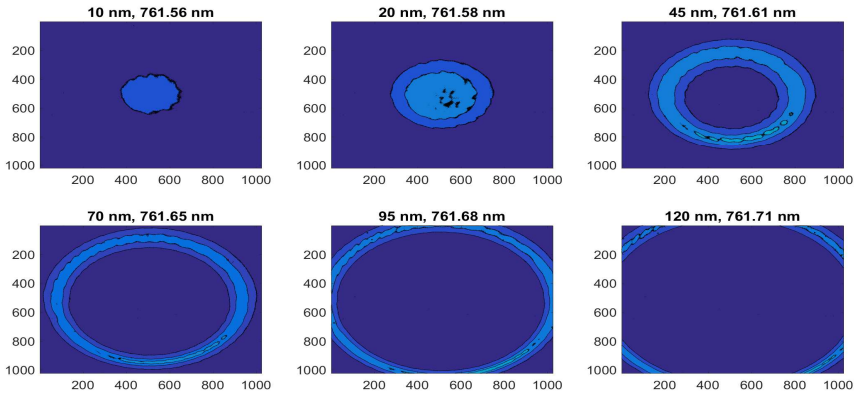

Fig. 3.7: Fringes generated from the F-P

3.4 Determine the variation of the finesse across the etalon

Here, the same setup was used as in the previous sections, with the only difference being a small aperture with a diameter of 5 mm. This small pinhole was part of an adjustable board that can move in the horizontal and in the vertical direction relative to the clear aperture of the Fabry-Perot. The board, as is shown below, was positioned between the interference filter and the etalon and was painted black so as to minimize stray light reaching the cavity. The pinhole aperture was moved 10 mm away from the center of the clear aperture of the etalon, in all 4 directions, including the center position.

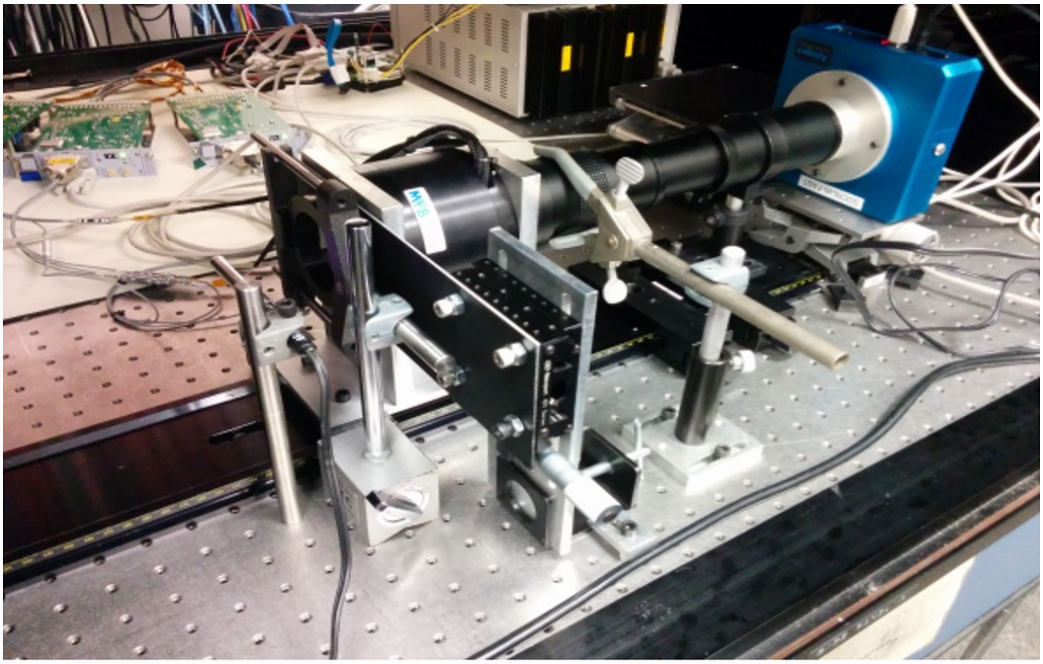

Fig. 3.8: Setup with aperture in front of F-P

For each position of the aperture, a step scan was performed with a range of 1000 nm, in gap spacing units. The piezo readings started at (410, 426, 576 nm) and incrementing with a 10-nm step increased until (1410, 1426, 1576 nm) for each sensor respectively. Because the camera sensor has a total of 1024 x 1024 effective pixels, a different value of reflectivity Finesse can be derived from each of these individual pixels. Thus, a 2-D map representing the variation of the Finesse across the etalon area can be produced, for each position of the aperture. This is shown below:

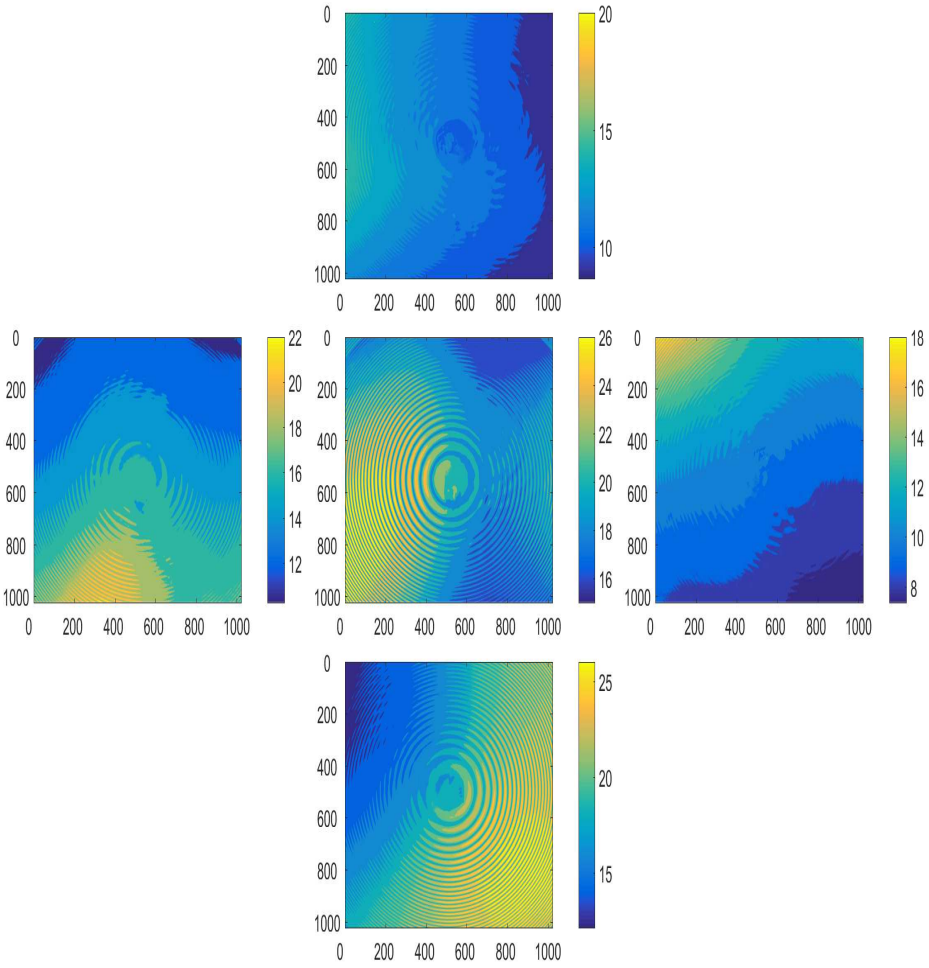

Fig. 3.9: Setup with aperture in front of F-P

Each of the images in Fig. 3.9 does not correspond to raw images but is rather a representation of the Finesse for each pixel calculated from the step scans. A Lorentzian fit was applied to each pixel, which in turn corresponded to one individual scan and the Finesse was determined for all

1024 x 1024 pixels of the CCD. The different patterns for all 5 images makes it clear that there is a noticeable change in Finesse as we go to off-axis angles.

By comparing the background colors for each image, the Finesse variation can be determined across the aperture. For the bottom, left and center images there is a fine fringe pattern across the CCD and the Finesse experiences a rapid change with off-axis angles. However, in the top and right images the Finesse varies slowly as we move off-axis, which is as expected. It is also important to note that the higher values of Finesse appear when the aperture was positioned at the center of the etalon, with a mean value of 23, whereas for the right position the Finesse is the lowest with an average value of 9.

3.5 Determine the initial spacing between the plates and the order of interference for the centre fringe

From data produced from the previously mentioned step scans, an image was selected where two fringes (interference rings) are visible on the

detector screen. In the Fig. 3.10 a centre bright fringe is noticeable, along with an outer ring which is partially distinguishable on the four corners of the CCD. The small aperture that was included in the previous setup was positioned at the left of the center of the clear aperture of the etalon and the piezo readings were 250, 550 and 670 nm respectively.

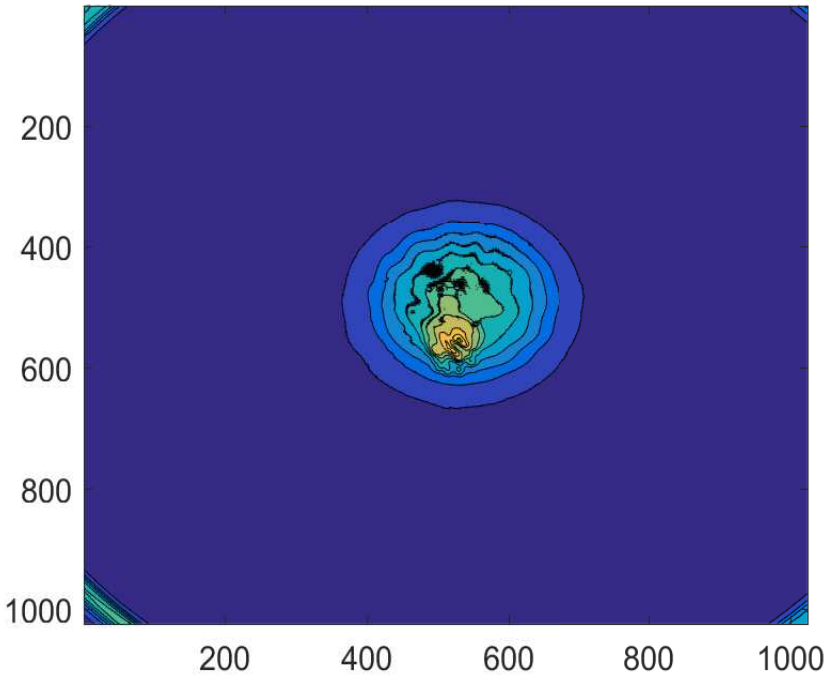

Fig. 3.10: The centre fringe is concentrated in a small bright area and the second ring is only visible from the corners of the detector

Since two rings are visible there will be two conditions that have to

be met for constructive interference. For the centre fringe, the equation that is applied is $m\lambda$=$2d\cos\theta_0$, where θ_0 is the half angle that is subtended by the ring ($\theta_0 \approx 1$), m is the order of interference and d the gap spacing. The focal length was set to a value of f=420 mm throughout all the tests, as mentioned in previous sections and since monochromatic light was assumed with a peak wavelength of λ=739.39 nm emitted from the Argon source, this value remains unchanged across the image of the detector. Therefore, in order for the equation to be satisfied, the interference order m should decrease as the angle λ increases in value so that we get (m-1)λ=$2d\cos\theta$ for the outer ring. Subtracting these two equations we get λ=2d(1-cosθ), but for small angles (θ<1) as is the case for our setup, the cosine term is expanded and the equation becomes λ=$2d\frac{\theta^2}{2}$. The half angle subtended from the second fringe is θ=arc$tan^{-1}(r/f)$, where r is the distance from the center of the outer fringe to its edge. Since the CCD camera has a total number of 1024 x 1024 pixels, each one having a size of 24.24 μm, r=658.33 pixels or r=15.8 mm and θ=2.154 degrees and thus the physical gap spacing will be d=λ/θ^2=523.45 μm. The interference order is given by m=$2d/\lambda$=1414.

3.6 Optimal piezo readouts for improved parallelism

The goal here is to determine the best readouts for the three piezos in order for the spectrometer to produce the same fringe as the aperture is moved in the horizontal or in the vertical direction. Essentially, the expected result would be the values of the piezo readouts where there is a minimum variation in the diameter and maximum sharpness of the rings on the CCD. For this reason, the readout of piezo 2 was fixed at 550 nm and a scan was carried out by varying the readouts of piezo 1 and piezo 3, in order to find the best combination. The scan range was from 250 nm until 850 nm and the step size was 60 nm. This process was carried out with the aperture positioned at a certain distance left from the F-P, as well as in the right direction. The best correlation between the two images (left and right fringe) for every step is achieved if the piezo readings have values 430, 550 and 730 nm for Piezo 1,2 and 3 respectively. The value of the correlation coefficient in this case will be 0.6657. However, there is a minimum value of correlation when the piezo reading are set at 490, 550 and 250 nm and the correlation coefficient value is -0.3729. These results are shown below in Fig. 3.11 and Fig. 3.12:

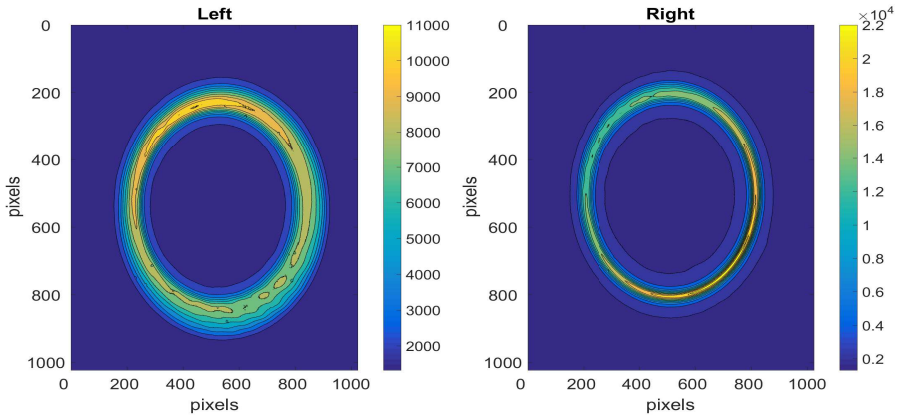

Fig. 3.11: The contour of the rings when the aperture was positioned at the left and right of the F-P. The images are very similar and the correlation is the largest (0.6657).

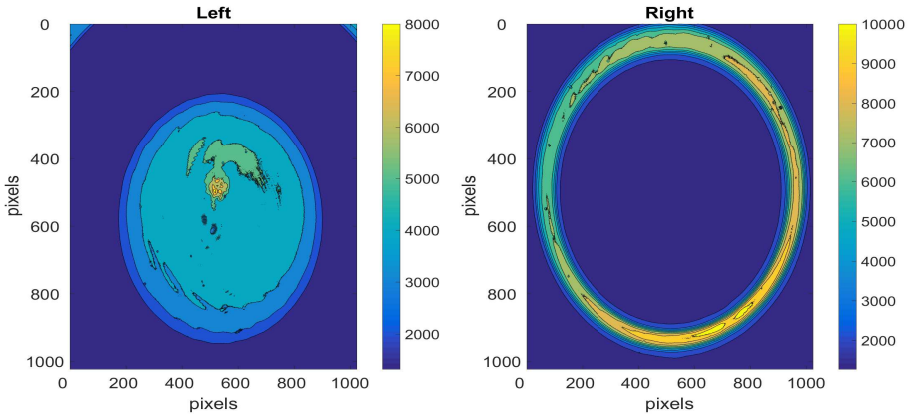

Fig. 3.12: The contour of the rings when the aperture was positioned at the left and right of the F-P. The images are very different and the correlation is the lowest (-0.3729).

The figure below is a 2-D grid representation of the correlation coefficient. The x-axis represents the displacement of Piezo 1 and the y-axis the displacement of Piezo 2. It is clearly noticeable that the yellow and orange areas yield the highest correlation and these areas correspond to piezo readouts in the range 670-730 nm for Piezo 1 and 310-370 nm for Piezo 2 respectively.

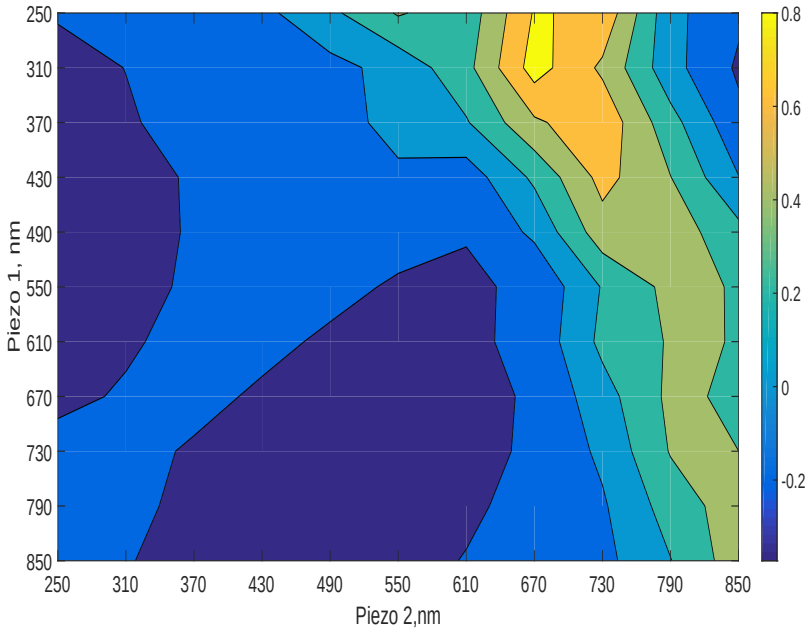

Fig. 3.13: The contour map of the 2-D correlation coefficient

The same process is carried out for the vertical direction, relative to the F-P. This time Piezo 3 remains at a fixed value of 579 nm and Piezo 1

and 2 change from 260 nm to 360 nm with a step size of 1 nm. The maximum correlation is achieved when the Piezos have readings 310, 334 and 583 nm and the minimum correlation for 306, 330 and 579 nm.

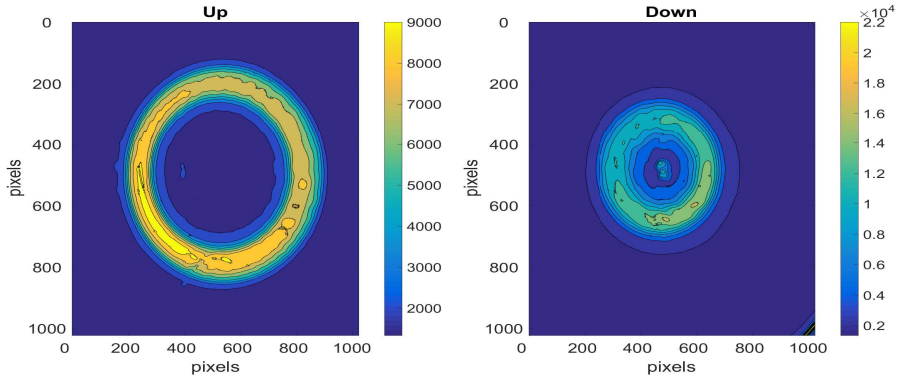

Fig. 3.14: Lowest correlation achieved (-0.0179) when the aperture was positioned up and down

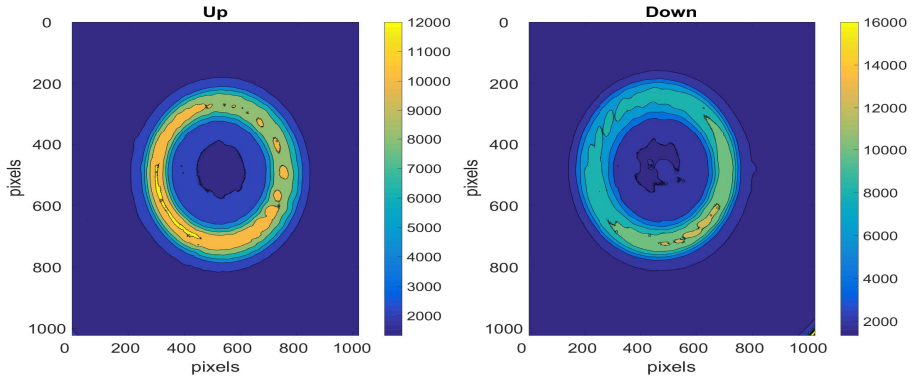

Fig. 3.15: Highest correlation achieved (0.6925) when the aperture was positioned up and down

Therefore, since the optimal readouts for the piezos were determined, the plates can be said to have a minimum deviation from parallelism when the piezo readouts are x_{piezo1},x_{piezo1}+24 nm, x_{piezo1}+273 nm which correspond to piezo 1,2 and 3, respectively. The variable which is used as reference each time a step scan is performed is x_{piezo1} and corresponds to the readout of the first sensor. Sensor readouts of 2 and 3 were determined by adding 24 nm and 273 nm respectively. Five step scans are now carried out, each corresponding to a different position of the aperture, so as to make sure the rings are highly correlated and the plates are therefore as parallel as possible. The range is 400-700 nm with an increment of 20 nm each time and the images are shown below for 5 different positions of the pinhole, for two different steps.

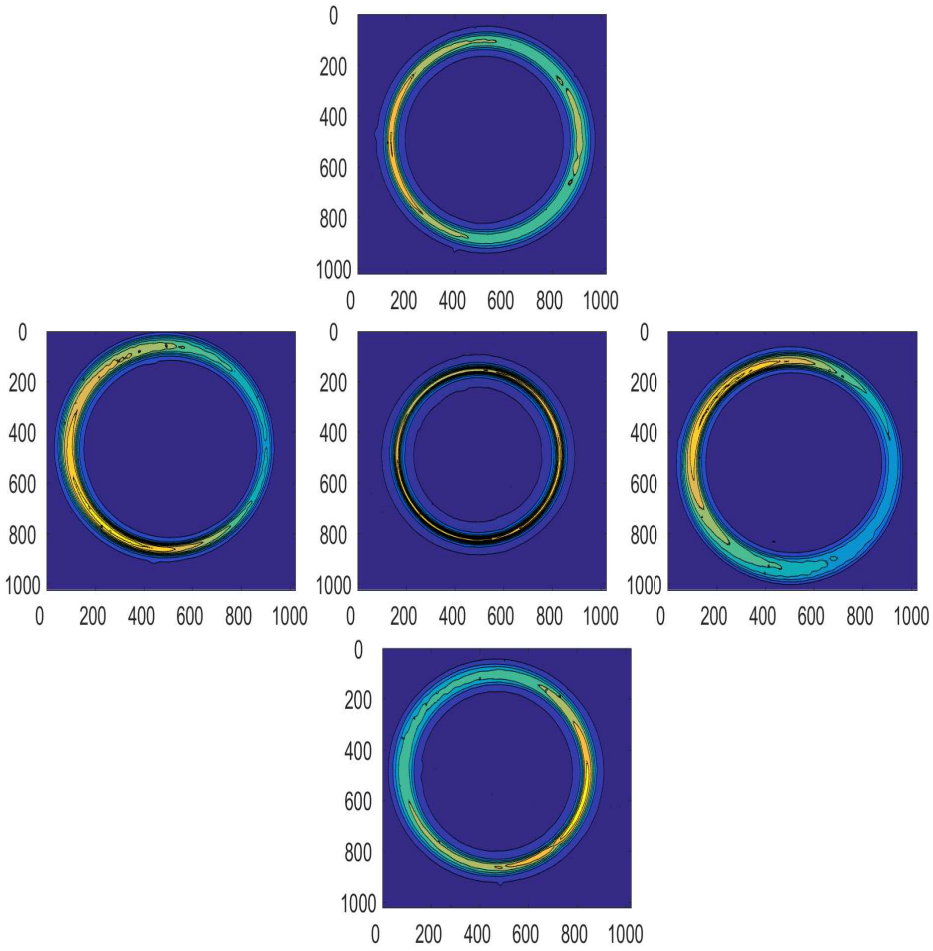

Fig. 3.16: The interference fringes that were produced by the F-P for five different positions (10 mm from the etalon centre) of the aperture (up, down, left, right, center). The sensor readouts are 380, 404 and 653 nm for each piezo respectively (The relative displacement is 80 nm).

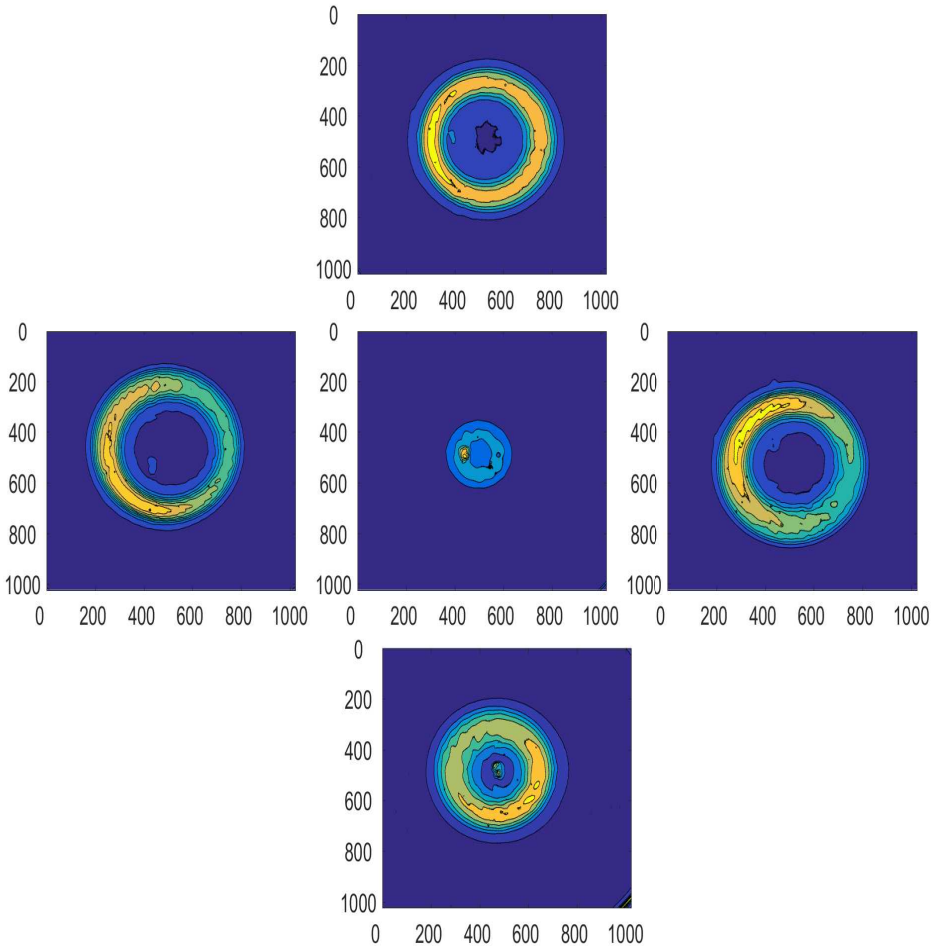

Fig. 3.17: The interference fringes when the readouts are 680, 704 and 953 nm.

Chapter 4

Re-calibration of the Fabry-Perot spectrometer

4.1 Modelling of the O_2 filters used during the flight

As described in the previous section, two custom-made bandpass filters provided by Andover Corporation were used throughout the flight, and their temperature dependence was tested and determined, with the use of a diffraction grating spectrometer. Each of these filters isolates a single free spectral range so that only one F-P peak is measured. However, since the

manufacturer could not supply a narrow enough passband width, two identical filters were used, narrowing the FWHM to the value that was desired. Important parameters regarding these two filters were provided by the manufacturer that helped in simulating the shape of the transmission curves and to better determine their performance with angular variation. These parameters were: the centre wavelength of the passband, the bandwidth at half the maximum intensity and the peak transmittance for a range of angles 0-1.5°. The effective refractive index is given n_{ef}=2.13 for both filters and the operating temperature is 23°C. Given the centre wavelengths at peak transmission along with the bandwidths for both filters at an incidence angle of 0 degrees the shape of the transmission curve can be determined by using the formula provided by Lissberger (1968) :

$$\tau = \tau(\lambda, \theta) = \tau_{max} \Big/ \left\{ 1 + \left[\frac{2(\lambda - \lambda_o)}{(\Delta\lambda)_o} + \frac{\lambda_o \theta^2}{(\Delta\lambda)_o n_{ef}^2} \right]^2 \right\} \tag{4.1}$$

The parameters involved in the above equation are defined below [17]:

- τ: transmission function of filter
- τ_{max}: maximum transmission
- θ: angle of incidence
- λ_o: wavelength at peak of curve for θ=0°

- n_{ef}: the effective refractive index of the filters

The transmission values for all three angles of incidence (0°, 0.97°, 1.5°) were produced based on this formula and in this way, the simulated values for the bandwidth and peak wavelength can be determined and compared with the ones provided by Andover. These values are presented in the tables below:

Table 4.1: Parameters for Filter 1, as were supplied by Andover

Angle (°)	**Filter 1**				
	Center Wavelength (nm)	**Simulated Center wavelength (nm)**	**FWHM (nm)**	**Simulated FWHM (nm)**	**Peak Transmission**
0	762.4105	-	0.167	-	0.4238
0.97	762.372	762.3864	0.168	0.1668	0.4101
1.5	762.3415	762.3529	0.165	0.1668	0.4072

Table 4.2: Parameters for Filter 2

Angle (°)	**Filter 2**				
	Center Wavelength (nm)	**Simulated Center wavelength (nm)**	**FWHM (nm)**	**Simulated FWHM (nm)**	**Peak Transmission**
0	762.4045	-	0.169	-	0.457
0.97	762.3885	762.3804	0.167	0.1688	0.4382
1.5	762.3615	762.3469	0.167	0.1688	0.415

From the above table, it is noticeable that the simulated values experience a very low deviation from the parameters supplied by the manufacturer. Specifically, the error present in the centre wavelength is $\delta\lambda$=0.012 nm, as opposed to the bandwidths that have an error of δB=0.0015 nm, which is negligible. Therefore, the Lissberger model yields trustworthy results and

provides a very accurate estimate of the transmission values for both filters.

Since the purpose of the bandpass filters is to transmit a well-defined band of light and reject unwanted radiation, their behavior strongly resembles a Fabry-Perot interferometer. Their design consists of a thin film that is essentially two highly reflecting mirrors separated by a layer of a dielectric material. Just as in the case for the Fabry-Perot, the centre wavelength of the filter will shift to lower values when light rays strike the surface at an angle θ bigger than 0 degrees, relative to the normal. This is best described from the following [18]:

$$\lambda_\theta = \lambda_o \Big[1 - \Big(\frac{n_o}{n_{ef}} \Big)^2 \sin^2\theta \Big]^{1/2} \tag{4.2}$$

where n_o is the refractive index of the medium surrounding the filters (assuming it is air, n_o=1.0002729) and the parameters λ_o, θ and n_{ef} are mentioned above. Therefore, a broadband filter can be tuned to the centre wavelength of our desire, assuming that collimated light is used and that the incident angles do not exceed 15 degrees.

The centre wavelength at different angles can therefore be easily calculated with the use of this formula, so based on this, the wavelength values

that we get at incident angles of 0.97 and 1.5 degrees are $\lambda_{0.97}$=762.3864 nm and $\lambda_{1.5}$=762.3529 nm and $\lambda_{0.97}$=762.3804 nm and $\lambda_{1.5}$=762.3469 nm for the first and second filter respectively. These values are the same as the simulated ones that were determined by using the Lissberger formula, therefore this is the method that will be used in order to determine the angular variation of the interference filters used during the flight measurements.

The simulated shape of the curve for both filters for three different angles of incidence using the model provided by Lissberger is shown below:

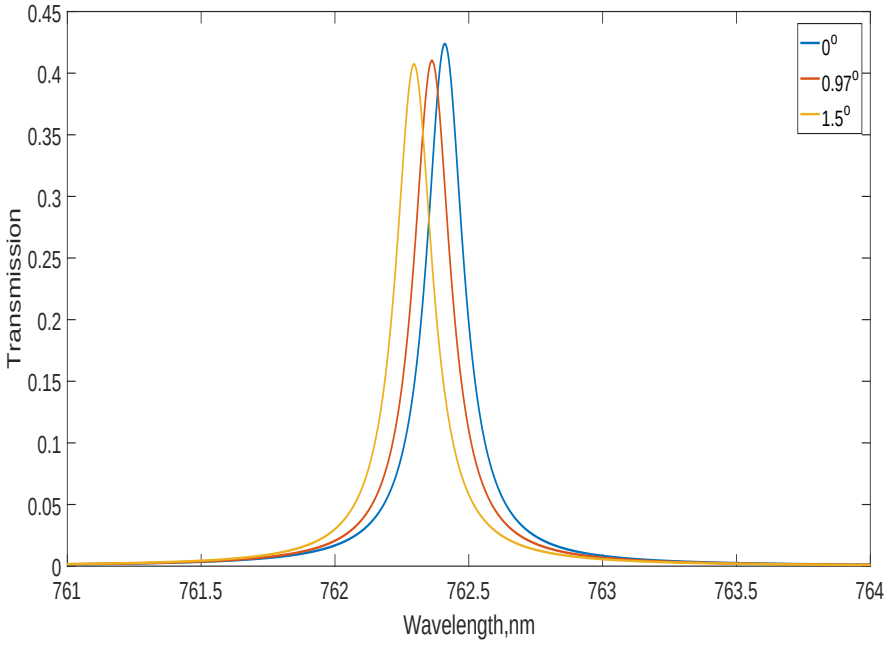

Fig. 4.1: Filter 1 simulated passbands

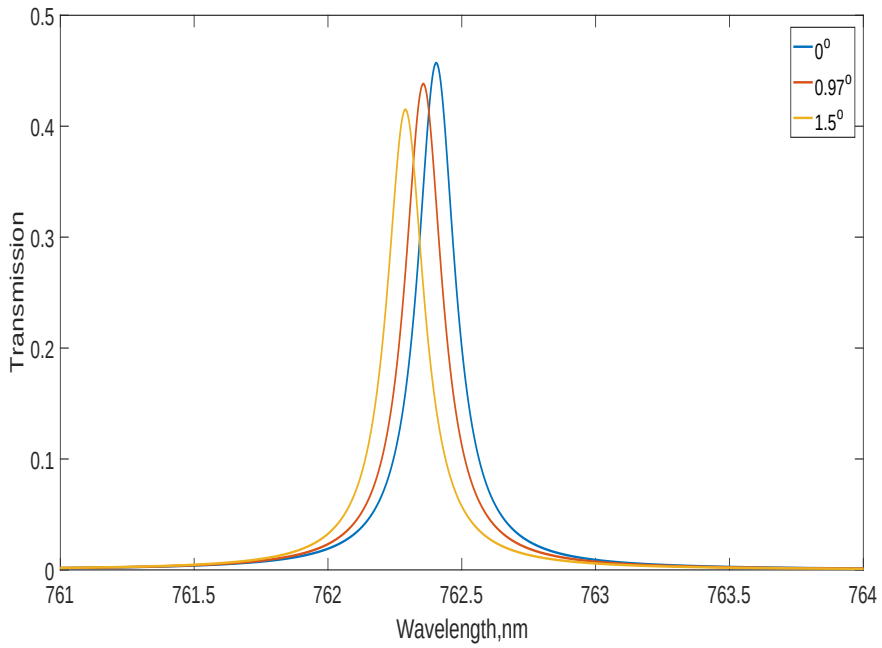

Fig. 4.2: Filter 2 simulated passbands

When both of the above interference filters are placed adjacent to each other inside the front optics tube, the total peak transmission decreases and becomes T=0.1932, the wavelength at peak transmission λ=762.4075 nm and the bandwidth FWHM=0.1083 nm.

4.2 Testing the temperature dependence of the Fabry-Perot

4.2.1 Using a thermocouple

In this test, it will be determined in what way the change in temperature inside the etalon will affect the output. Thus, the goal is to estimate whether there will be any noticeable shift in the peak wavelengths, as a result of a change in temperature. The components of the optical setup for this were:

- An Argon source
- A front lens with a pinhole aperture positioned at its focal point
- An interference filter with a maximum transmission at 739 nm
- The Fabry-Perot spectrometer
- A 420-mm telephoto lens
- A 1MP CCD camera

An external heater was used to control the temperature inside the system enclosure, along with a thermocouple that would measure the tem-

perature of the F-P. This resulted in a closed loop system, where temperature changes were recorded. The temperature was set to an initial value of 24.2°C and increased up to 30.3°C with a step of approximately 1°C each time. A step scan was carried out at each individual temperature with a step size of 10 nm and a 30 second exposure. The range was 400-990 nm, in terms of relative displacement, which is essentially the readings of the piezos throughout the scan.

Isolating an area of 10 by 10 pixels around the centre of the detector (512,512), step scans were generated for all temperatures as a function of the piezo readings and also as a function of the wavelength. In order to convert the gap spacing to units of wavelength the equation $\lambda = \frac{2nd\cos\theta}{m}$ is used, where λ is the wavelength of the light entering the etalon, n the refractive index ($n \approx 1$), d the gap spacing, θ the angle through the etalon and m the order of interference. The initial spacing between the mirrors is assumed to be $d = 557\mu$m and the order of the center fringe is $m = 1464$ and therefore the following graphs are generated:

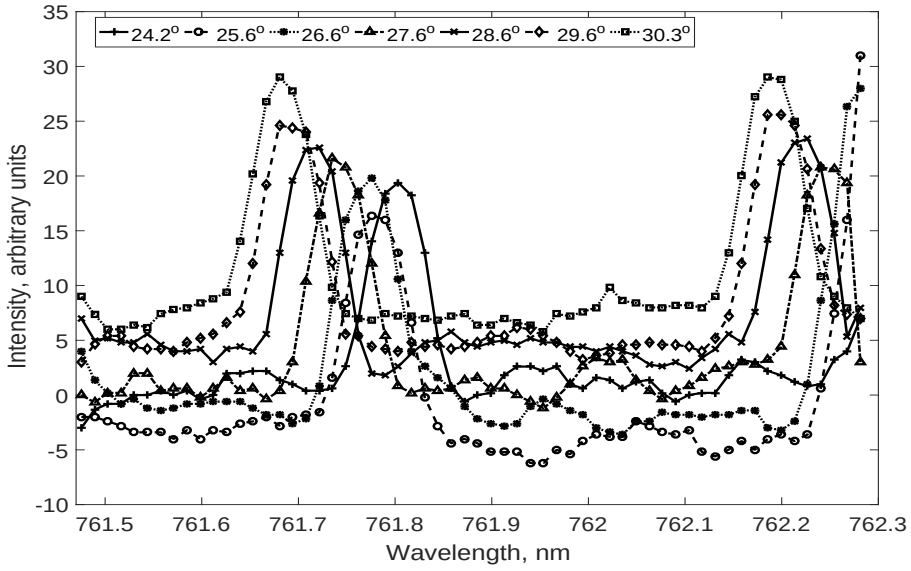

Fig. 4.3: Transmittance versus wavelength as a function of temperature

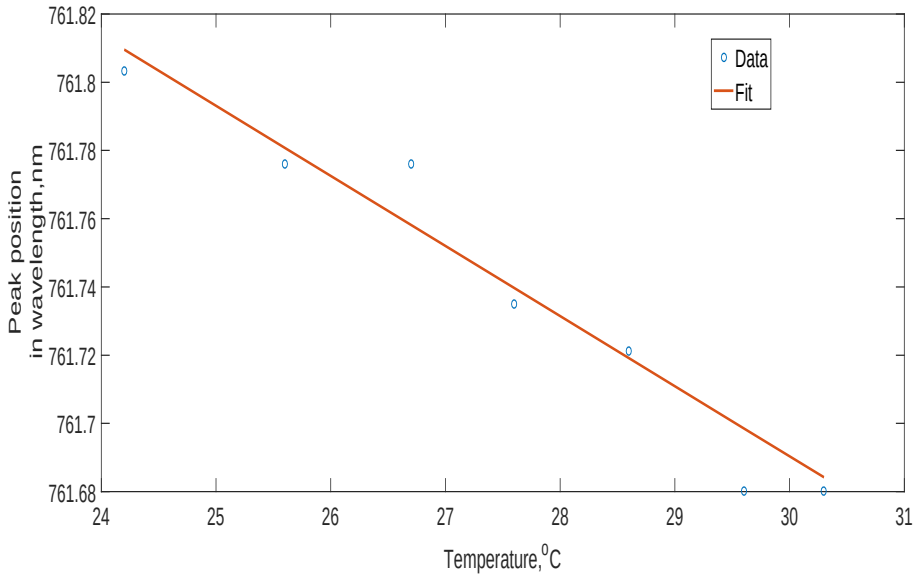

Fig. 4.4: Change in wavelength with temperature

In Fig. 4.3 the step scans generated for each temperature. A filter was applied in order to define the centre of the peaks more accurately. Fig. 4.4 shows how the wavelength shifts to smaller values as the temperature increases. The change is close to linear so applying a fit we get a shift of 8.75 nm/°C in gap spacing units or 0.0206 nm/°C in wavelength units.

4.2.2 Using a temperature controller

Here, the same setup is used, but instead of a thermocouple and an external heater a Minco temperature controller and two heaters were used and were attached to the surface of the Fabry-Perot. The DC temperature controller provided power to two Thermofoil heaters and an RTD (Resistance Temperature Detector) sensor. The temperature of the spectrometer was controlled by adjusting a set point and monitoring the output signal temperature using a multimeter. The output of the signal was 10 mV/°C. The temperature range this time was 24.7-33.8°C, the scan range 400-995 nm and the step size 5 nm and therefore:

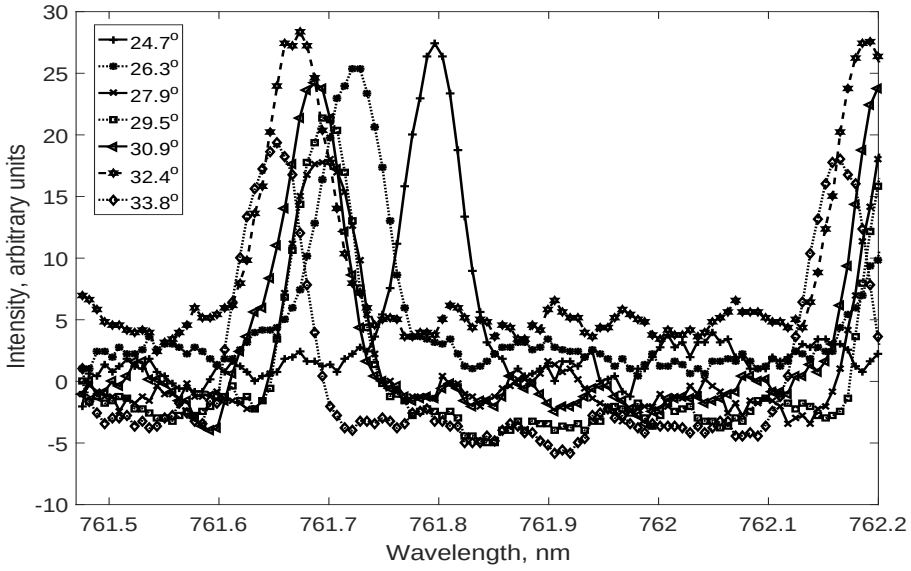

Fig. 4.5: Transmittance versus wavelength

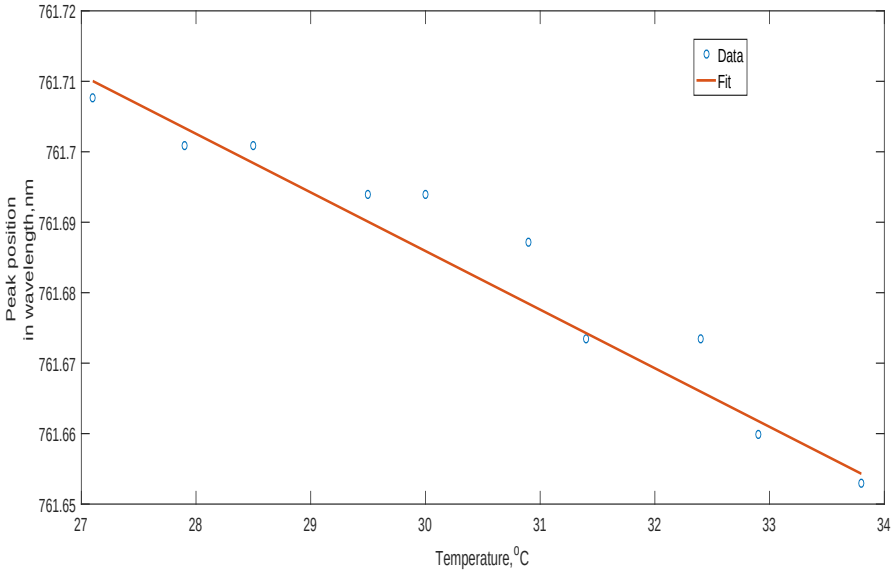

Fig. 4.6: Change in wavelength with temperature

For both methods, an hour was needed in between each measurement for the temperature to stabilize at a certain value. It is quite noticeable that in the range 24.7-25.7°C there is a large decrease in wavelength of 0.048 nm, as well as in the range 25.7-26.3°C with a value of 0.023 nm. This is probably due to the fact that the temperature is constantly changing at these low values so temperature values above 26.3°C are only taken into account. The temperature coefficient for this method is estimated to be 0.0129 nm/°C.

4.3 Calculate the linear dispersion of the diffraction grating

The main purpose of this test was to analyze the passband of the O_2 filters that were used for the balloon flight campaign, as well as test their performance over changing temperatures. For this reason the experimental setup was different than the one that was previously used and included:

- A SPEX diffraction grating spectrometer
- A 1kW light source with a Tungsten filament

- A 50-mm Nikon lens, used to image the light source onto the entrance slit of the spectrometer
- The Argon interference filter
- A Nikon D7000 camera

The SPEX model of the spectrometer is basically a Czerny-Turner monochromator consisting of two narrow slits, two curved mirrors and a diffraction grating. A schematic of the basic optical layout of this intrument is provided below, with A and B being the entrance and exit slits respectively [19]:

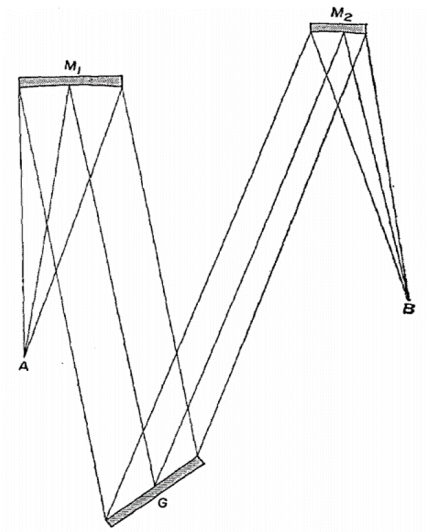

Fig. 4.7: Optical layout of a Czerny-Turner monochromator. M_1 and M_2 are the mirrors and G represents the grating.

The power supply of the Tungsten source was set to 8 Amps and the width of the entrance slit of the spectrometer was decreased to 0.5 mm. The exit slit width was set to 0 mm and was completely covered, so that no light could pass through. The detector (Nikon camera) was placed vertically facing downwards at the reflecting mirror of the spectrometer. The spectrometer scans by rotating the grating with the use of a wavelength screw. The screw was manually rotated until light was seen on the detector, and this was at a wavelength reading of 1517 nm. The scan was done +/-20 nm around this spectral line with a step of 5 nm so the range was 1497-1537 nm. The actual wavelength of the incident light is determined by dividing the wavelength reading by 2.

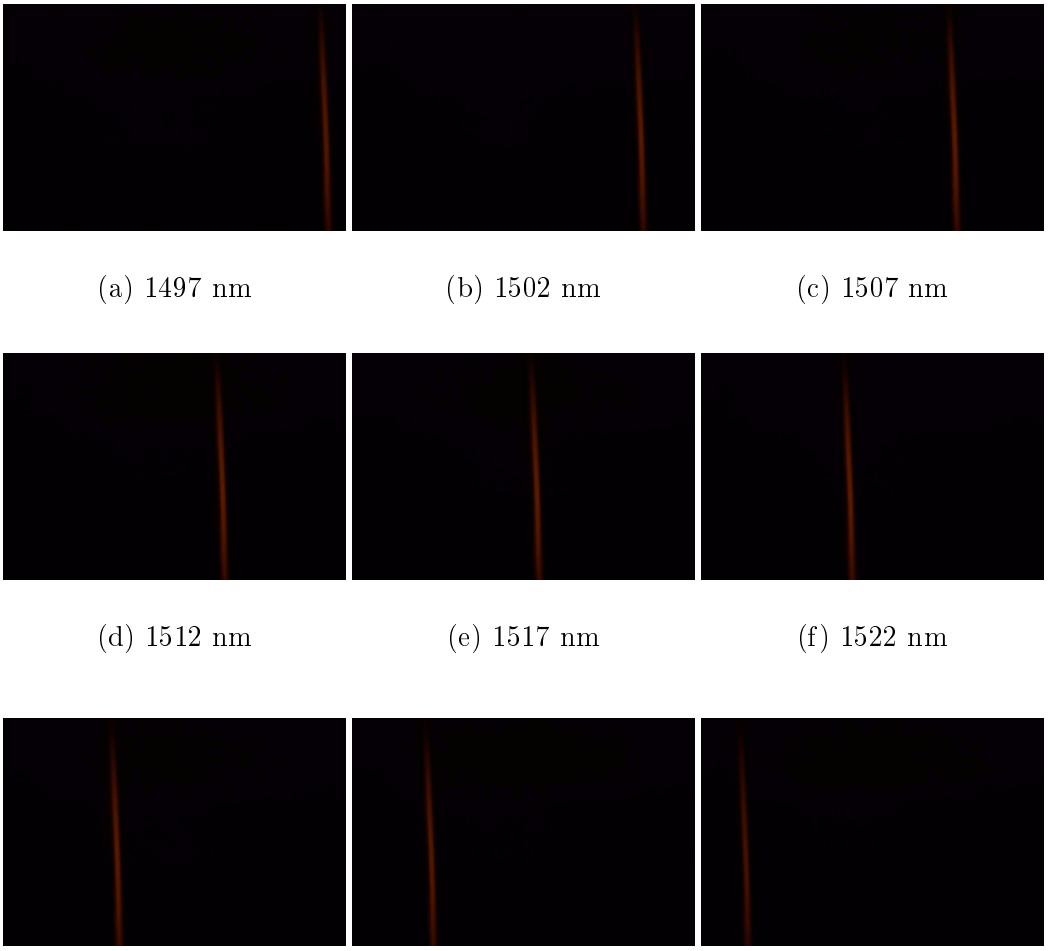

(a) 1497 nm (b) 1502 nm (c) 1507 nm

(d) 1512 nm (e) 1517 nm (f) 1522 nm

(g) 1527 nm (h) 1532 nm (i) 1537 nm

Fig. 4.8: Change in position of the spectral line as the grating rotates.

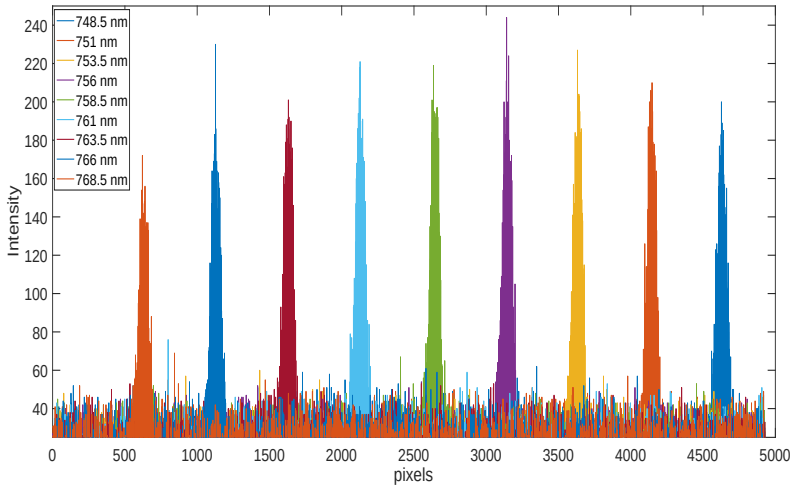

Fig. 4.9: Diffraction grating spectra versus pixel number for different wavelengths

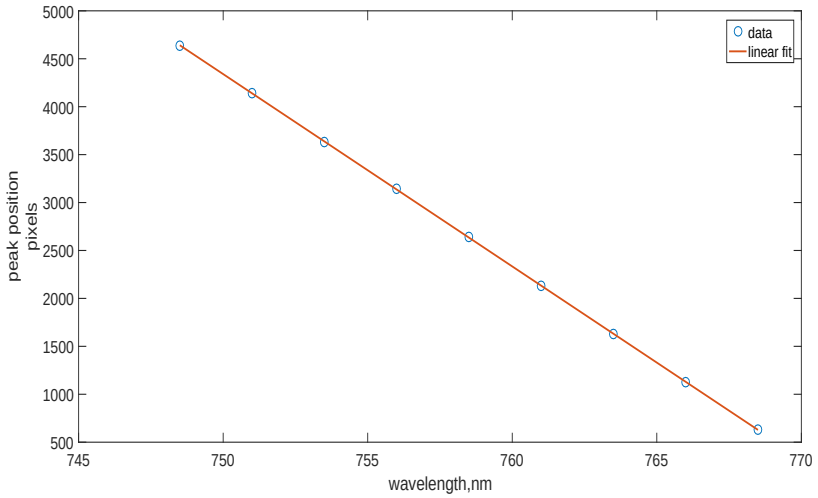

Fig. 4.10: Shift in peak position versus wavelength change

The peak position is plotted against the wavelength and applying a linear fit a linear dispersion is estimated at 200.48 pixels/nm.

4.4 Determine the temperature dependence of the filters

For this test, the setup that was used was the same as the one previously mentioned, with the only difference being the optical tube that enclosed the two O_2 filters, which was placed at the entrance slit of the spectrometer, as seen below:

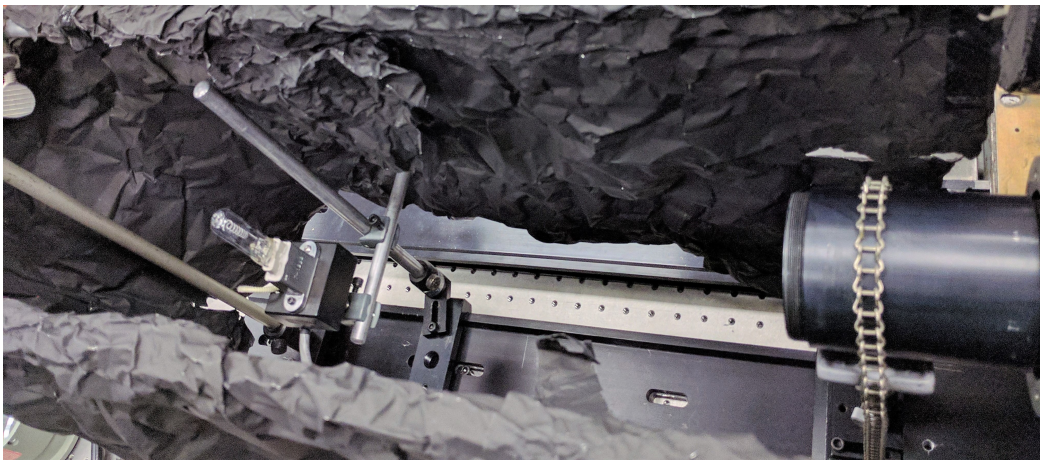

Fig. 4.11: Top view of setup showing the optical tube and the Tungsten source

The distance between the Tungsten source and the entrance slit was increased, as excess heat from the Tungsten filament might have affected the filter's performance. The Argon filter, as well as the front 50-mm lens were not included in this setup. The Minco temperature controller was also used and the heaters were placed on the tube. The temperature was controlled by adjusting the set point of the controller and increased from room temperature at 24°C until 69°C with a step of 5°C each time. 30 minutes were needed between each measurement for the new temperature to reach the filters and stabilize.

The Nikon camera has a number of effective pixels of 16.2 million and an image area of 4928 x 3264 pixels. In order to get the spectra for each temperature all the horizontal spectra were added from row 1000 until row 2000 to obtain a larger signal of 10^4 magnitude. A Gaussian fit was applied to each individual temperature spectrum and the plots are generated:

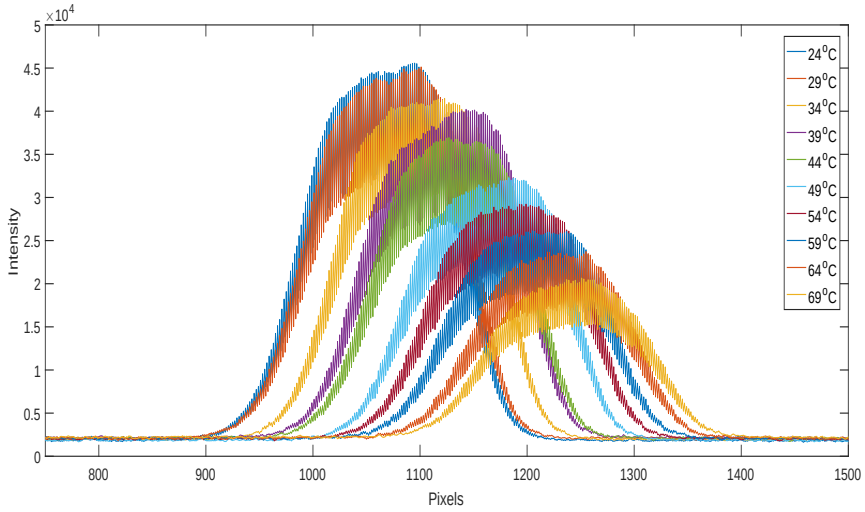

Fig. 4.12: Transmittance versus pixel number

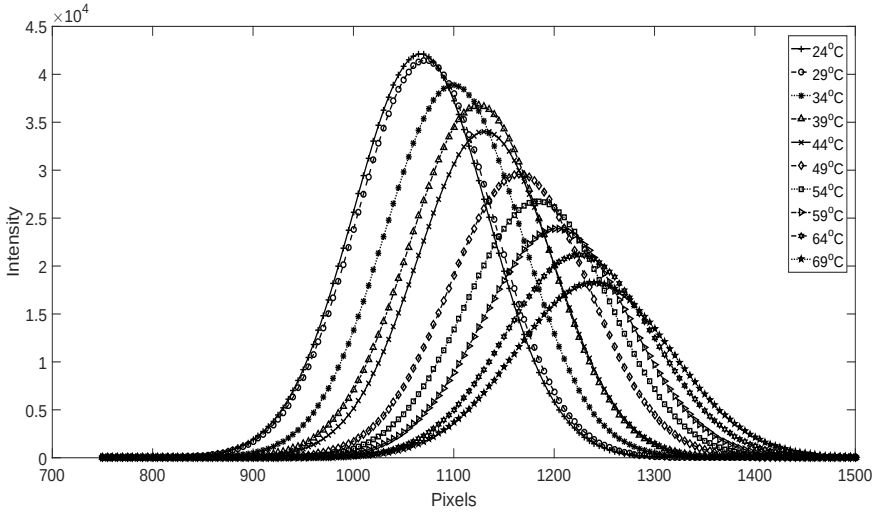

Fig. 4.13: Gaussian fit for each step scan

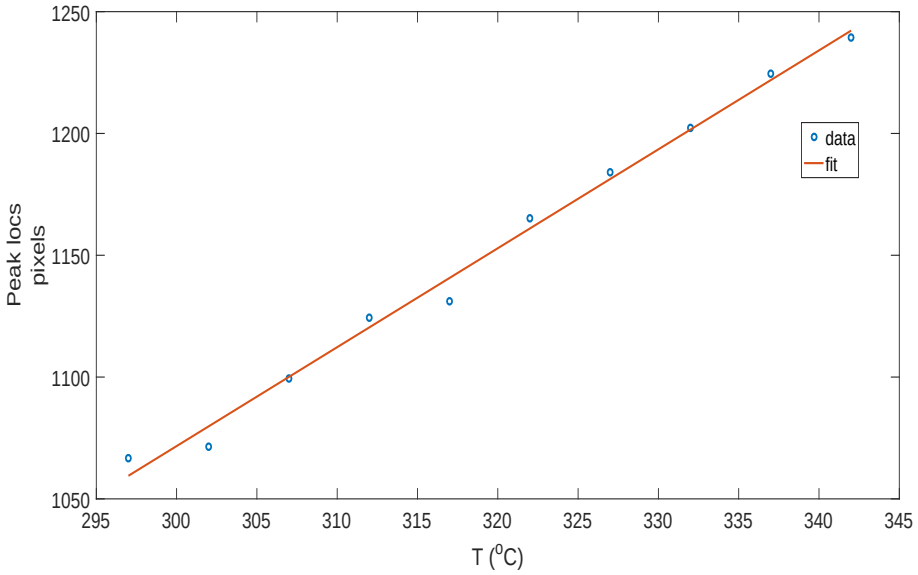

Fig. 4.14: Peak shift versus temperature change

The position of the peaks (in pixels) was plotted against the changing temperature and applying a linear fit, the linear equation that was generated was $P = 4.06T - 146.59$, where P is the peak (pixels) and T the temperature (°C). The change is estimated to be ΔP=4.06 pixels/°C or $\Delta\lambda$=ΔP$\frac{1}{\text{dispersion}}$ and therefore $\Delta\lambda$=(4.06 pixels/°C)$\left(\frac{1}{200.48 \text{ pixels/nm}}\right)$=0.0203 nm/°C, as the linear dispersion was found to be 200.48 pixels/nm. The size of each pixel of the camera is 4.78 μm × 4.78 μm so the actual linear dispersion will be (200.48 pixels/nm)(4.78 μm/pixel)=958.29 μm/nm or $\frac{dL}{d\lambda}$=0.0958 mm/Å.

Thus, the reciprocal linear dispersion will be $\frac{dL}{d\lambda}$=10.438 Å/mm.

An expression can also be derived for this quantity if we take into account some parameters related to the diffraction grating spectrometer. The fundamental grating equation that can be applied here is described as follows [20]:

$$m\lambda = d(\sin\alpha + \sin\beta) \tag{4.3}$$

where m is the spectral order, λ the wavelength of interest, d the groove spacing and α, β are the incident and diffracted angles respectively. In the case of this particular SPEX 1700 model, since the focal length of the collimating mirror is 750 mm, the angles can be expressed as α=θ+ϕ and β=θ-ϕ, where ϕ=6.8583° and θ being the rotation angle of the grating, as measured from the zero point, when looking directly at the image. So the incident wavelength as a function of θ can be written as:

$$\lambda(\theta) = \frac{d[\sin(\theta + 6.8583) + \sin(\theta - 6.8583)]}{m} \tag{4.4}$$

The groove frequency is G=$\frac{1}{d}$=1200 gr/mm so the spacing between the grating rulings will be d=$\frac{1}{1200gr/mm}$=0.83 μm/gr and the order of diffraction is m=1. So taking a range of angles from $\theta = 0°$ to $\theta = 70°$ with

an increment of dθ=0.001, we get the different wavelengths that correspond to them, as is better understood from the graph below :

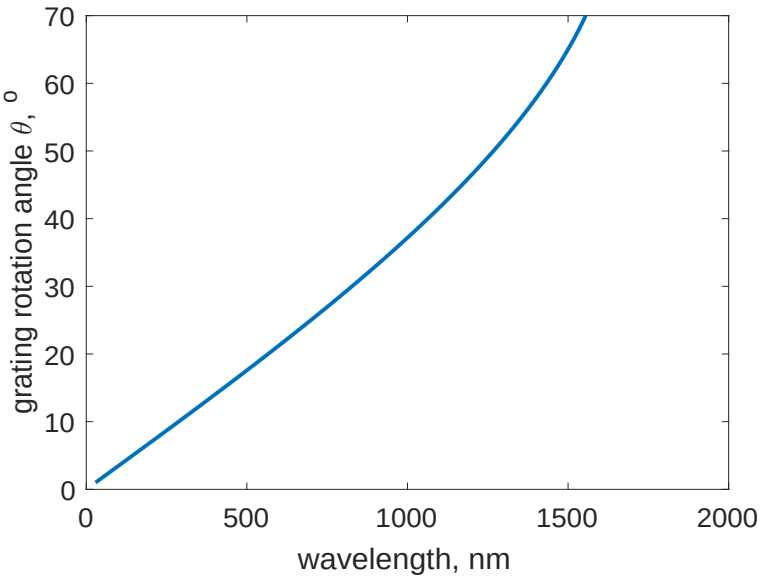

Fig. 4.15: Angle of rotation of diffraction grating versus incident wavelength

The curve shown above exhibits a linear behavior for angles 0-50°, so it is found that for a wavelength of 762.4 nm the rotation angle will be θ=27.435 degrees, or in terms of the angle of diffraction β=27.435-ϕ=20.576 degrees. Using this value and the parameters that were mentioned previously, the reciprocal linear dispersion can be calculated based on the equation [19]:

$$\left(\frac{dL}{d\lambda}\right)_{theory} = \frac{d\cos\beta}{mf} \tag{4.5}$$

All the above parameters are known now so if we input them into Eq.

(4.5) we get $\left(\frac{dL}{d\lambda}\right)_{theory}$=10.4023 Å/mm.

4.5 Determining the O_2 filter passband

An attempt was made to calculate the spectral passband and shape of the interference filters used in the previous test. The experimental setup remains unchanged, with the only difference being the temperature, which is set to 25°C (room temperature, the heaters are turned off). The reading on the wavelength counter on the diffraction grating spectrometer is adjusted to 15240 Å (762 nm in actual wavelength) so that the spectral line is centered on the detector. The width of the entrance slit is varied from 0.07 mm to 0.4 mm with an increment of 0.05 mm each time and an image is taken for every individual measurement. The spectrum is plotted versus pixel number for the horizontal middle row of the image and a Gaussian fit is applied to all images, as is shown in Fig. 4.16 :

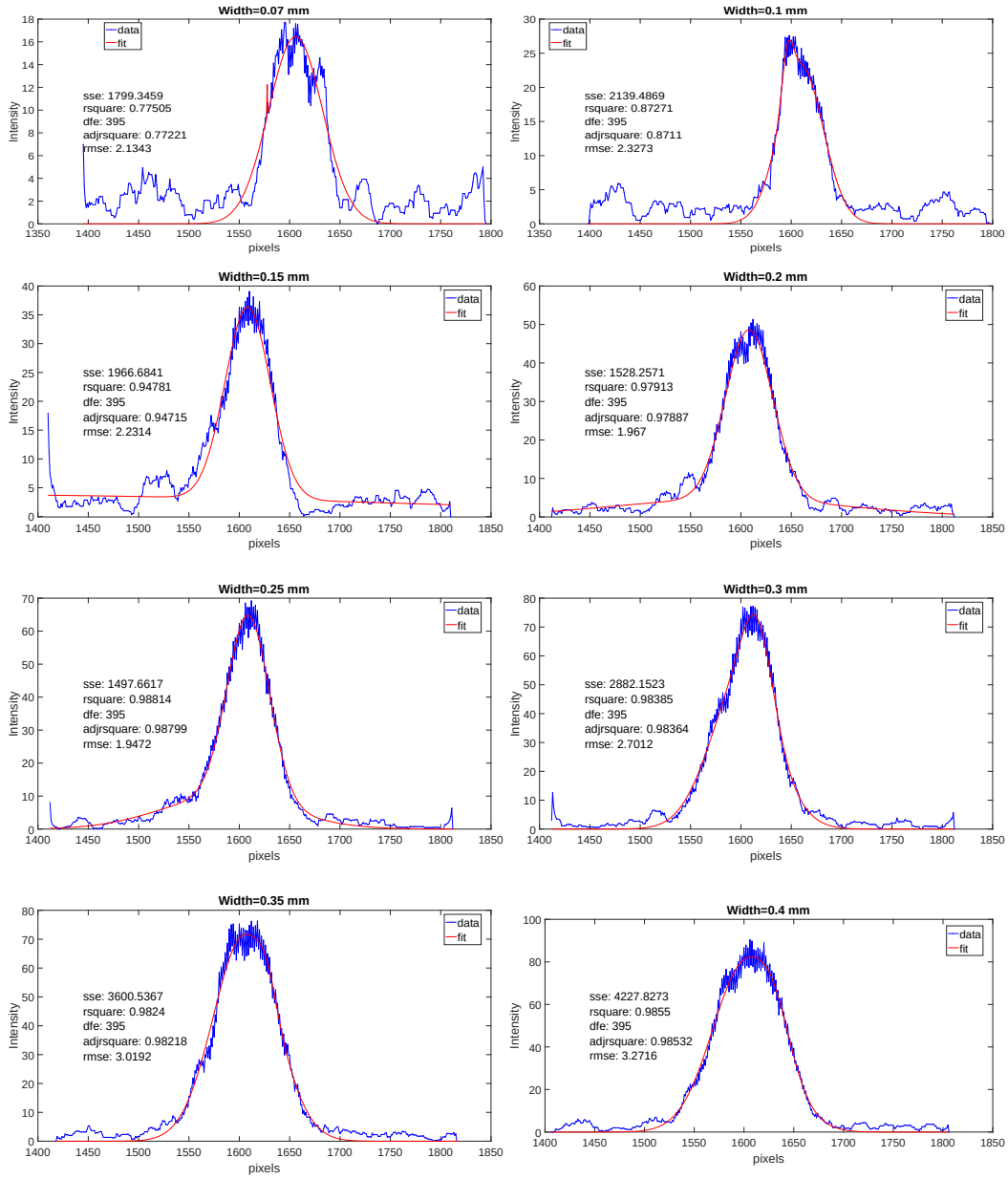

Fig. 4.16: Observed spectra of filter for different entrance slit widths (0.07-0.4 mm)

From the above figures, it is clear that the best fit is achieved when the width of the entrance slit is w=0.2 mm, with a correlation coefficient R=0.97913 and a RMSE (Root mean square error) of rmse=1.967. There was a considerable amount of background noise, possibly due to stray light coming into the spectrometer and a measurement of dark current was not done (the images are not dark corrected). Therefore, a moving average lowpass filter is used in order to smooth the data and get a better fit. The FWHM of this recorded spectrum after fitting the data with the Gaussian function is $FWHM_{rec}$=55.35 pixels. The linear dispersion is 200.48 nm/pixels so the bandwidth in wavelength units will be $FWHM_{rec}$=(47.91 pixels)(1/200 nm/pixels)=0.239 nm.

As no spectrometer is perfect, the spectral output can be characterized as a line spectrum having a finite width, which is known as the instrumental line profile. The result of this is the apparent spectral broadening of the purely monochromatic wavelength emitted from the light source, caused by the spectrometer. The parameters that influence the shape of the instrumental line profile are the following:

- The width of the entrance slit
- The width of the exit slit or the width of one individual pixel, if a

camera is used as a multichannel detector

- Phenomena related to diffraction and different types of aberrations, such as spherical aberration and astigmatism

- Experimental errors that have to do with the quality of the spectrometer and the setup alignment

The emission is assumed to be monochromatic and the experimental tests were done with a high-resolution spectrometer, so the instrumental bandpass will depend on the entrance and exit slits, ignoring any diffraction and aberration phenomena. The entrance slit has a width of 0.2 mm, and the pixel used as the exit slit has a width=4.78μm, much smaller in size than the entrance slit, therefore the instrumental passband, dominated by the entrance slit will be given by [20]:

$$BP_{instr} = D * w \tag{4.6}$$

where D is the linear dispersion (the dispersion at the focal plane) D=10.438 Å/mm and w=0.2 mm the width of the entrance slit so a passband value of BP_{instr}=0.208 nm is obtained. The bandpass (or full width at half maximum) of the total recorded spectrum, assuming Gaussian distributions, will be given

from the following formula [13]:

$$BP_{rec} = \sqrt{BP_{line}^2 + BP_{instr}^2 + BP_{res}^2} \tag{4.7}$$

where BP_{line} is the spectral width of the natural line associated with the emitting source (afer accounting for the effect of the filters on the transmitted light), BP_{res} is the resolution of the instrument that limits the performance of the spectrometer and BP_{instr} is the instrumental passband that was previously calculated. From theory, it is well known that the resolving power for a diffraction grating is given by [20]:

$$R = \frac{\lambda}{\Delta\lambda} \tag{4.8}$$

where λ=762.4 nm is the wavelength of the emitting source and $\Delta\lambda$ the limiting resolution. If the number of grooves N being illuminated on the surface of the grating is known, then the resolving power in the diffraction of order m becomes [20]:

$$R = mN \tag{4.9}$$

The width of the grating that was used is W=110 mm and since the groove density is n=1200 gr/mm, for a first order diffraction (m=1) the resolving power will be R=Wn=(110 mm)(1200 gr/mm)=132000. Rearranging we get a resolution of $\Delta\lambda = BP_{res} = \frac{\lambda}{R}$=(762.4 nm)/(132000)=0.0058 nm.

Since $BP_{res} \ll BP_{instr}$ the contribution of the limiting resolution of the instrument to the total passband can even be ignored.

Having calculated the spectral widths associated with the recorded spectrum (BP_{rec}), the instrumental profile (BP_{instr}) and the limiting resolution (BP_{res}), the width of the line source can now be determined, which will be a good estimate of the filter passband. From Eq. (4.7) we get:

$$BP_{line} = \sqrt{BP_{rec}^2 - BP_{instr}^2 - BP_{res}^2} = 0.1176nm \tag{4.10}$$

So the spectral width of the interference filter will then be $FWHM_{filter}$=BP_{line}=0.1176 nm, which actually corresponds to the bandpass resulting from a combination of two filters positioned side by side. Based on the documentation supplied by Andover and the calculations in previous sections, this value at normal incidence should be ≈0.1083 nm according to theory, but which differs slightly from the bandwidth calculated by an error of δ=0.0093 nm. This may possibly be due to certain errors related to the experimental setup such as:

- Possible misalignment of the emitting source with the interference filter and with the spectrometer
- The emitted radiation from the Tungsten filament might strike the surface of the filter at an angle, resulting in a wavelength shift, and

thus a different recorded spectrum through the spectrometer

- Stray light significantly influenced the results and might have been the main reason behind the noisy transmission values

- The limiting accuracy of the reading of the entrance slit width (in mm), resulting in an altered instrumental passband

One last significant factor that should be taken into account is that although the temperature these tests were conducted at was 25°C, a wavelength shift is present, since the operating temperature of the filters is set to 23°C. However, given the temperature coefficient calculated from previous sections (0.02 nm/°C) the change in center wavelength would be $\delta\lambda$=0.04 nm, which will not contribute significantly to the overall spectrum. The Tungsten lamp though will increase the temperature of the surrounding medium due to heat radiated at a current of I=6A, and therefore alter the transmission peak.

The shape and bandwidth of the filters can also be determined by performing a deconvolution of the recorded spectrum F_{ob} , assuming that the instrumental passband yields a rectangular function F_{ob} with a spectral width of BP_{instr}=0.208 nm, determined from above. The equation that is

used involves the convolution:

$$F_{ob} = F_{instr} * F_{line} \tag{4.11}$$

where F_{line} is the shape of the line spectrum that is attempted to be retrieved. However, this kind of procedure is not straightforward in Matlab and doesn't give good results. For this reason, the real part of the FFT (Fast Fourier Transformation) is obtained for the observed and instrumental passband and performing an inverse transformation (iFFT) we get the estimated filter transmission curve:

$$F_{line} = iFFT\left(\frac{FFT(F_{ob})}{FFT(F_{instr})}\right) \tag{4.12}$$

Based on this, the resulting transmission curve is:

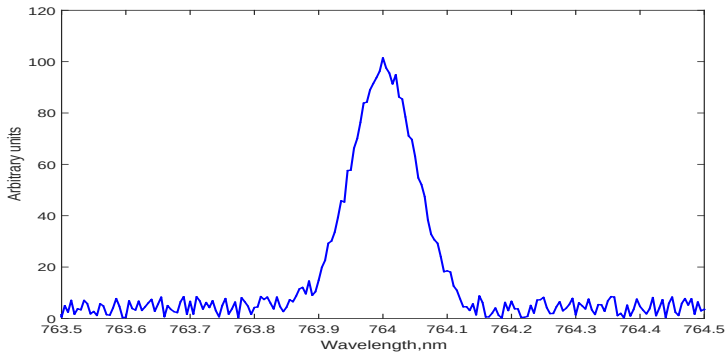

Fig. 4.17: Transmission curve for the filters, generated from an inverse transformation

Applying a Gaussian fit a passband of $BP_{line,ifft}$=0.1224 nm is obtained, which differs from BP_{line}=0.1176 nm by $\delta\lambda$=0.0048 nm. This is possibly because a rectangular function was assumed for the instrument, which gives different results.

4.6 Spectrometer wavelength calibration

The goal here is to get an estimate of the offset due to the reading of the wavelength counter, on the diffraction grating spectrometer. The setup doesn't change, but the front optics tube, the O_2 filters and the Tungsten lamp are replaced by the Argon lamp and the interference filter at 739 nm. A step scan is performed for five different wavelengths and we get:

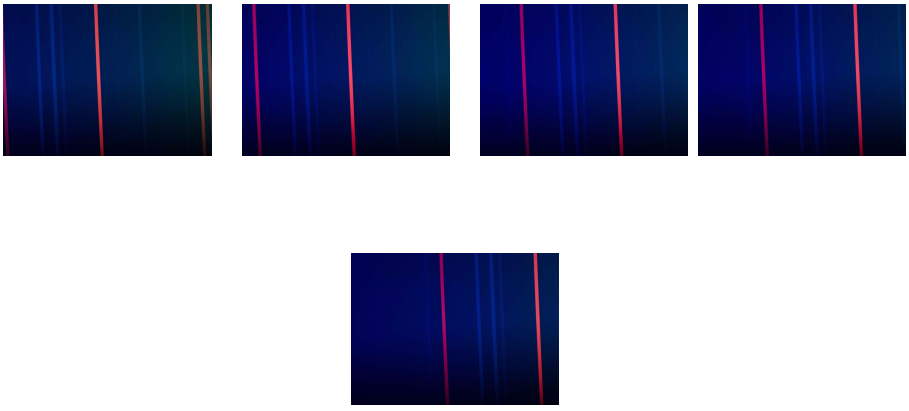

Fig. 4.18: Change in position of the spectra as the grating rotates.

Making use of the equation λ=λ_o+(dλ/dλp)p_{peak} the actual wavelength is determined that is assumed to correspond to the bottom left corner of the image. dλ/dλp is the reciprocal linear dispersion ($\frac{1}{200}$ nm/pixel), p_{peak} the position of the peak of the spectra and λ the wavelength of the light source (λ=738.38 nm). Plotting λ_o against the spectrometer reading an offset of 2 nm is obtained, which is a relatively large value:

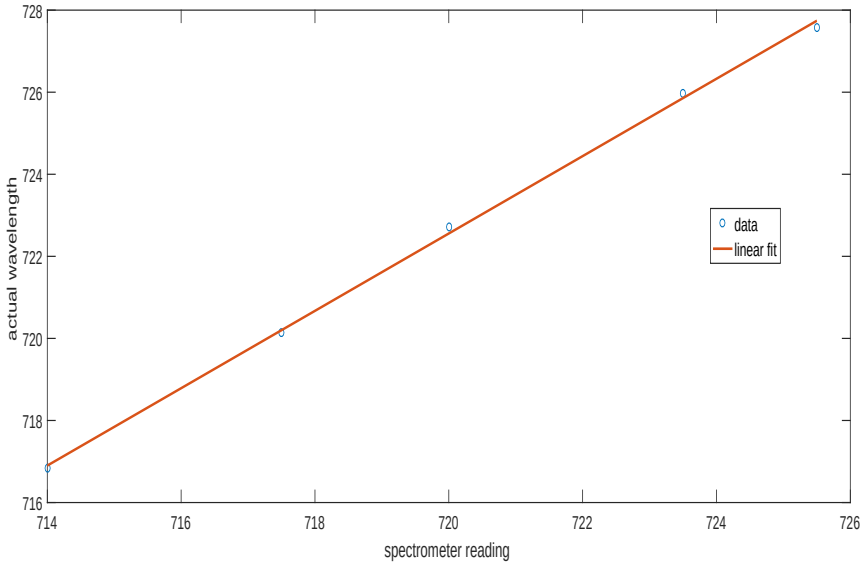

Fig. 4.19: True wavelength versus wavelength from spectrometer reading

4.7 Creating a 2-D map representing the change in gap spacing

The goal that wanted to be achieved here was to estimate the imperfections associated with the flatness of the mirror plates of the F-P. In order to do that the following setup was used:

- An argon light source
- A 50-mm Nikon lens
- A small aperture along with a collimating lens
- An interference filter
- The Fabry-Perot
- A 40-mm Nikon micro lens
- A Nikon D7000 camera

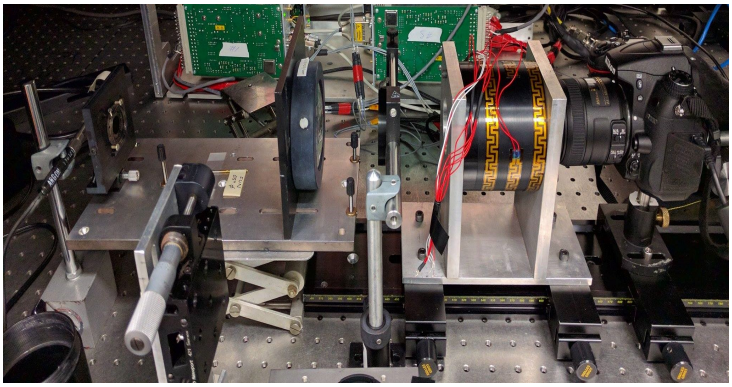

Fig. 4.20: Optical setup to generate a gap spacing map

The front lens is used to image the lamp on the aperture, which has an adjustable opening and was set to 16 mm. As shown in Fig. 4.20, the aperture is positioned at the front focal plane of the collimating lens, having an effective focal length of 20 cm. Therefore, the etalon throughout this test is imaged onto the detector, whereas for the previous measurements and the flight instruments the light is collimated through the etalon. A step scan was performed with a range 200-800 nm (in piezo readings) and a step size of 5 nm. The exposure time was set to 10 seconds and the f-number of the camera lens was fixed at f/2.8 (f-number range is f/2.8-f/22).

A smaller area of 500 by 400 pixels is isolated onto the detector that had the largest intensity and the peak position for each step scan at each pixel position was determined:

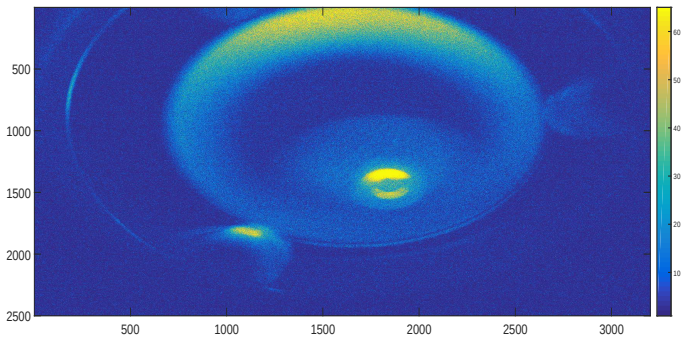

Fig. 4.21: 2-D contour of etalon

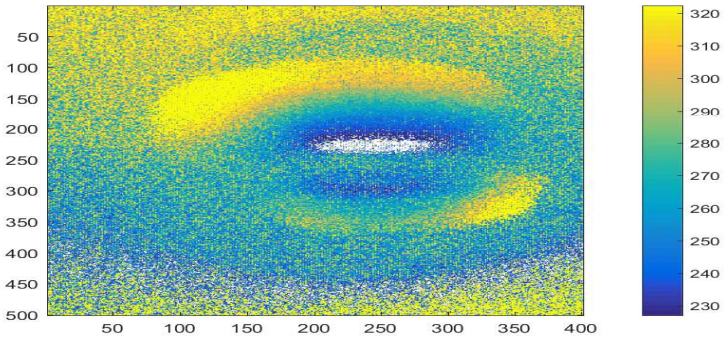

Fig. 4.22: 2-D gap spacing map, 500 x 400 pixel area

In this way, a gap spacing map was created depicting the variation in peaks, in units of gap spacing, which was done for all step scans across the sub image. From the figures, there is a noticeable decrease of approximately 60 nm in the values as we go towards the lower region of the image.

Fig. 4.21 shows the raw image of the entire surface of the etalon. As step scans were performed on the spectrometer, the only pixels that varied

in intensity were those within an area of 500 x 400 pixels. This corresponds to (1100-1600) and (1700-2200) in pixel units in the vertical and horizontal direction of the CCD image represented in Fig. 4.21. Fig. 4.22 clearly shows this isolated area after having done a step scan for each element on the image. Each pixel has a different value of the peak position of the scan, in units of piezo readings. The color variation in the image indicates that there is a gradient in the gap spacing of the etalon in the vertical direction.

4.8 Calibration and responsivity calculation of the flight instrument

The purpose of these measurements was to allow the absolute radiances of the flight observations to be determined. The setup that was used here included the Fabry-Perot attached to the telescope lens and the CCD camera at one end and the optical tube with the interference filters and front optics at the other end. The 1 KW Tungsten lamp was positioned at a distance of z=50 cm away from the centre of a diffuse reflective surface at an angle of α=10 degrees. This is the angle between the screen and lamp axis. The instrument was also placed a certain distance from the screen in a way

that it's entire field of view was uniformly illuminated.

In Fig. 4.23 shown below, values of irradiances and reflectances are provided for different wavelengths, for the Tungsten lamp:

Wavelength [Å]	Irradiance [#photons / cm^2 s Å]	Irradiance [mW / m^2 nm]
3000	2.50864 x 10^{10}	1.66323
3100	3.69681 x 10^{10}	2.37192
3200	5.23677 x 10^{10}	3.25498
3300	7.24319 x 10^{10}	4.36567
3400	9.79227 x 10^{10}	5.72848
3500	1.29415 x 10^{11}	7.35449
3600	1.67399 x 10^{11}	9.24877
3700	2.13774 x 10^{11}	11.49182
3800	2.69263 x 10^{11}	14.09381
3900	3.33435 x 10^{11}	17.00517
4000	4.07353 x 10^{11}	20.25562
4500	9.34056 x 10^{11}	41.28528
5000	1.73395 x 10^{12}	68.97640
5550	2.90009 x 10^{12}	103.93302
6000	3.97636 x 10^{12}	131.81648
6546	5.33603 x 10^{12}	162.13524
7000	6.45602 x 10^{12}	183.44323
8000	8.58708 x 10^{12}	213.49618
9000	1.01746 x 10^{13}	224.85917
10500	1.12813 x 10^{13}	213.70087
11500	1.14098 x 10^{13}	197.34076
12000	1.13833 x 10^{13}	188.67887

(a)

Wavelength [Å]	Reflectance factors
3000	0.975
3500	0.981
4000	0.984
4500	0.984
5000 - 8500	0.986
9000	0.984
9500	0.986
10000	0.983
10500	0.986
11000	0.987
11500	0.985
12000	0.983

(b)

Fig. 4.23: (a)Certificate for the 1-kW tungsten lamp showing the calibrated values of irradiance for a wavelength range from 3000 Åto 12000 Å. (b)Calibrated reflectance factors for the same wavelength range

The values in Fig. 4.23a and Fig. 4.23b were obtained at a distance

of x_o=50 cm from the screen. Based on the lamp certificate, it is possible to determine the irradiance of the source for a wavelength of 762.4 nm, which is the center wavelength of the interference filters where the transmission is at its maximum. The most straightforward way would be to use a linear interpolation method, which would give an irradiance of $I_{\lambda,interp}$=7.819e+12 #photons cm^{-2} s^{-1} nm^{-1}. However, a more accurate way would be to use a fit that gives the spectral irradiance as a function of the wavelength, with two parameters in the equation. The mathematical model was developed by Saunders at NIST and is given by [12]:

$$I_{\lambda,Saunders} = \lambda^{-5} e^{(\alpha - \beta\lambda^{-1})} \tag{4.13}$$

This fit makes use of the least squares method, where λ=762.4 nm and α=81.53, β=54340 are the fitting parameters. The calibrated values along with the fitting curve for the spectral range of the Oriel lamp are shown below [21]:

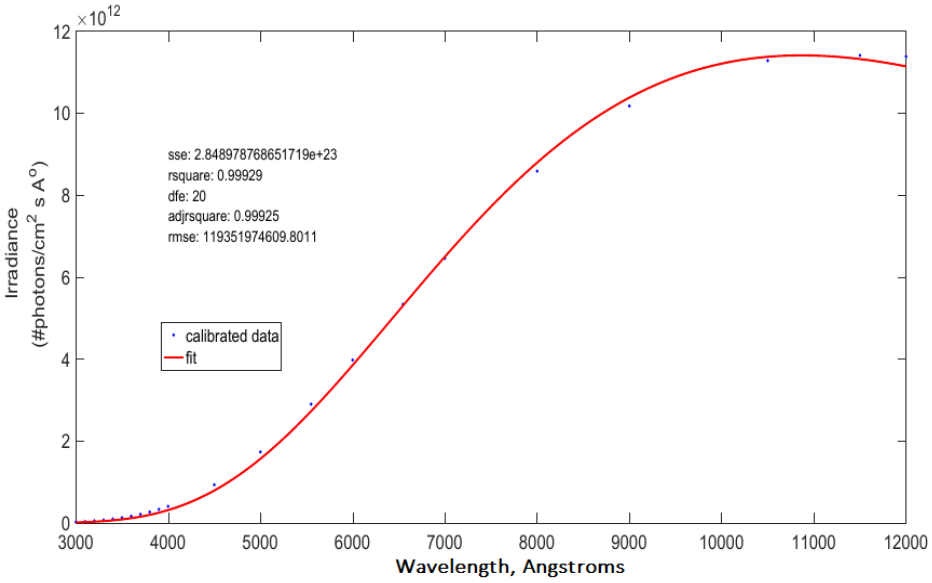

Fig. 4.24: The calibrated irradiance values along with the fit provided by Saunders

From Fig. 4.24 and using the fitting equation, we obtain an irradiance value of $I_{\lambda,Saunders}$=8.542e+13 #photons cm^{-2} s^{-1} nm^{-1} or in energy units $I_{\lambda,Saunders}$=227.71 mW m^{-2} nm^{-1} .

The lamp is treated as a point source, meaning that the radiation is being emitted in all directions and isotropically. Therefore the square law can be applied here in order to calculate the irradiance at a distance greater than x_o=50 cm as follows:

$$I_{x\lambda} = I_{o\lambda}\left(\frac{x_o}{x}\right)^2 \tag{4.14}$$

where $I_{x\lambda}$ and $I_{o\lambda}$ are the irradiance values at distances x and x_o respectively. At a distance of x=60 cm we get $I_{x\lambda}$=5.9319e+13 #photons cm^{-2} s^{-1} nm^{-1}. From Fig. 4.23b the reflectance of the diffusing screen can be determined, since the reflectance factor remains relatively unchanged in most of the visible and near infrared spectrum (5000-8500 Å). Therefore, the reflectance of the screen at a wavelength of 762.4 nm would be ρ=0.986. The radiant exitance of a Lambertian screen is given by [21]:

$$M_\lambda = I_{x\lambda}\rho_\lambda cos\alpha \tag{4.15}$$

where $I_{x\lambda}$ and ρ_λ were determined from before and assuming that the angle between the normal to the screen and the point source is small $\alpha \approx 0^o$ we get an exitance of M_λ=5.8489e+13 #photons cm^{-2} s^{-1} nm^{-1} or M_λ=152.6 mW m^{-2} nm^{-1}. The radiation reflected off the diffusing screen is distributed isotropically in all directions so dividing the spectral irradiance M_λ with a factor of π would give the spectral radiance. Therefore, the radiance incident on the instrument is B_λ=$\frac{M_\lambda}{\pi}$=48.54 mW m^{-2} nm^{-1} sr^{-1}.

The step scan that was performed here had a range from 300 nm to 1200 nm, in piezo displacement, with a step of 20 nm and an exposure time of 1 second. Below, the entire step scan is shown, as well as the transmittance

at the certain spectral range of interest:

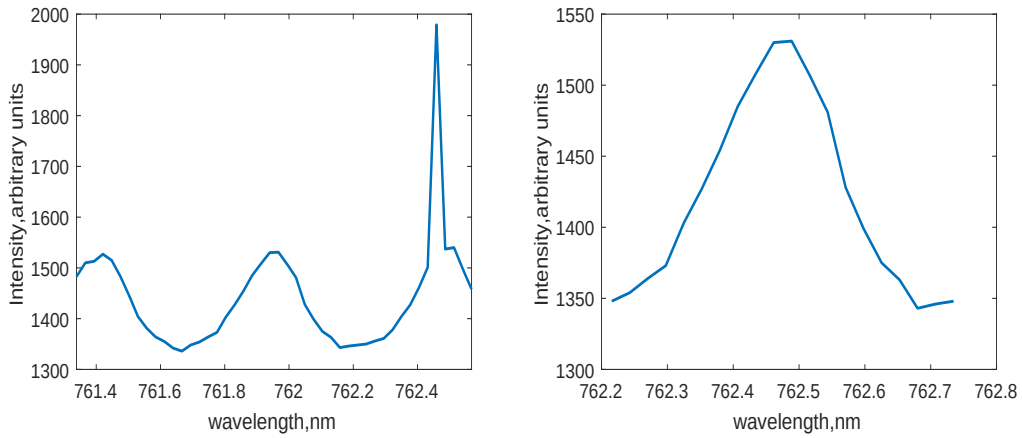

Fig. 4.25: (a)Step scan within a wavelength range of (761.35-762.5 nm). (b)Second-order peak curve representing the transmittance in the spectral range 761.7-762.2 nm.

As seen from above, the third peak shown in Fig. 4.25a exhibits a sudden increase in intensity. This is possibly due to secondary reflections within the surface of the etalon that contribute to this spike. Therefore, isolating the spectral range around the second peak and knowing the FSR=0.52 nm, the center wavelength becomes 762.47 nm, as shown in Fig. 4.25b. The maximum intensity for this step scan is I_{max}=1531 counts. The spectral radiance of the broadband source was previously found $B_\lambda = \frac{M_\lambda}{\pi}$=0.04854 W m^{-2} nm^{-1} sr^{-1}, so taking the ratio the maximum counts to this radiance

we get R=$\frac{I_{max}}{B_\lambda}$=31540 (counts/s)/ (W m^{-2} nm^{-1} sr^{-1}). This is the value of the responsivity that is retrieved for the instrument, which will help in converting intensity from counts to actual radiance units.

4.9 Characterization of the improved Fabry-Perot

A test had to be carried out for the Fabry-Perot spectrometer after its performance was improved by MPB. It was important to perform a step scan in order to get the instrumental passband and the reflectivity Finesse before the Alice Springs balloon flight campaign. The F-P spectrometer this time was enclosed in the sealed tube of the flight unit along with the telescope lens, the CCD camera, the interference filters and the front optical layout. The argon lamp is used as a light source and the exposure time is 1 second. A step scan is carried out with a step size of 5 nm and a range of 1200-2000 nm, in piezo readings units. Below, in Fig. 4.26 step scans are shown representing the transmittance as a function of wavelength, for different random angles of incidence.

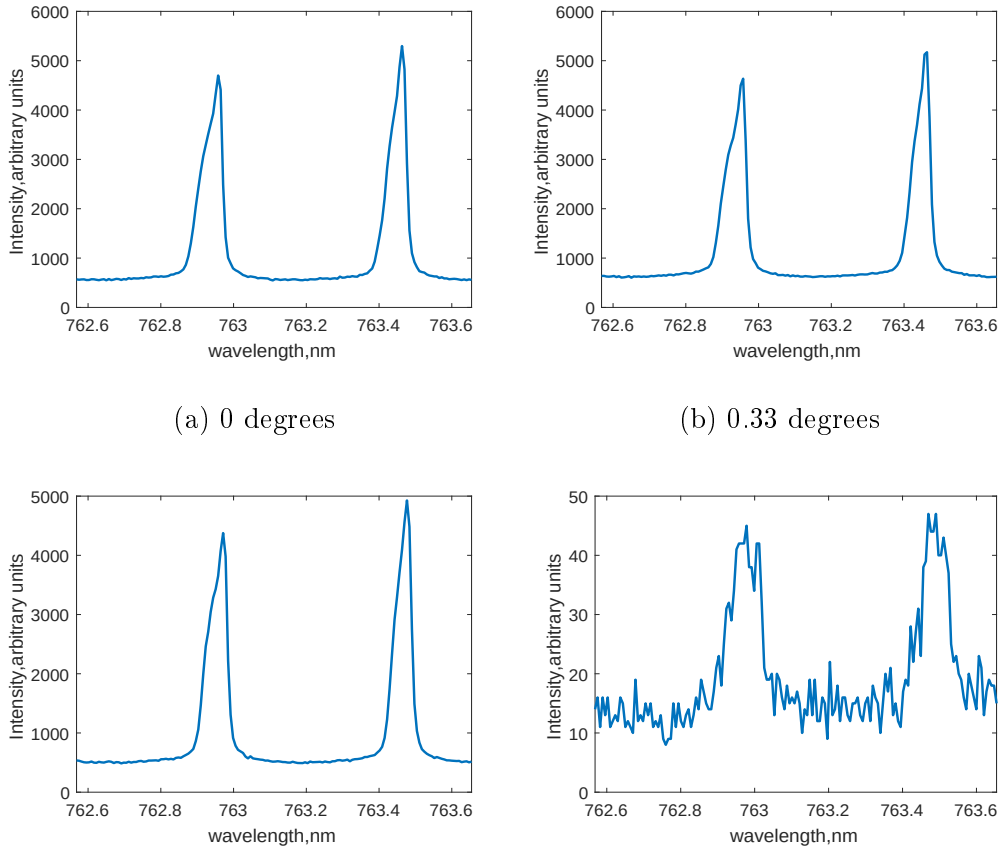

(a) 0 degrees

(b) 0.33 degrees

(c) 0.65 degrees

(d) 0.98 degrees

Fig. 4.26: Improved step scans for angles of incidence 0-0.98 degrees

Applying a Gaussian fit important parameters that are obtained are the free spectral range FSR=0.505 nm, a bandwidth of FWHM=0.052 nm and therefore a reflectivity Finesse of F=9.71, significantly higher than for the Kiruna flight. The shape of this instrumental passband will prove useful

in the calculations done in the following section, where an attempt is made to convolve the Airy function that was obtained with a narrow-line source with the atmospheric spectrum. The goal is to derive a spectrum that correlates strongly with the recorded spectrum that was produced during the balloon flight mission.

It is worth mentioning the mask design that was provided by MPBc for the Fabry-Perot etalon, in order to improve the instrument observations during flight. A gap-spacing map was generated, as was done in Section 4.7 and is shown in Fig. 4.27:

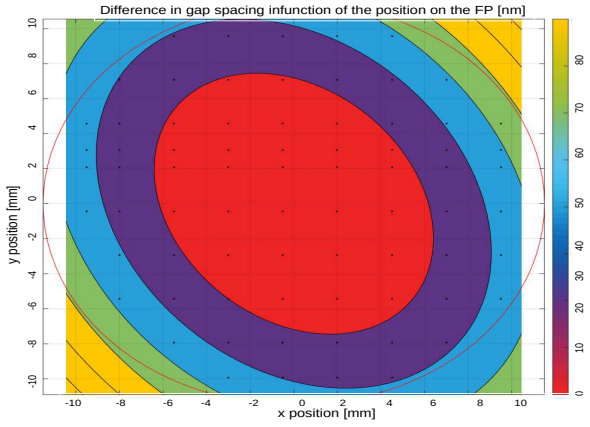

Fig. 4.27: Mask designed for the F-P by MPB Technologies Inc.

The mask that was made corresponds to the red region of Fig. 4.27,

where the variation in gap spacing is at its lowest. This region has a diameter of 12 mm, approximately half of the clear aperture of the F-P (23 mm). Although due to smaller aperture size, longer exposure times might be needed, this is not considered a serious limitation for the flight observations.

Chapter 5

Atmospheric observations during Alice Springs flight campaign

5.1 Recovering the true spectrum for the O_2 band from the observed spectrum

During the balloon flight in Alice Springs, Australia, 50 step scans were done throughout the total duration of the flight. The range was selected to be 400-761 nm, in piezo readings, since there is no point in going beyond the Free Spectral Range (≈380 nm, in relative displacement) to obtain useful data. The increment that was used between each measurement

was 19 nm with an exposure time of 30 seconds and a dark current measurement at the end of each individual scan. One of the main concerns was the temperature variation that was present for most of the duration of the flight. This was mainly due to the increasing altitude of the gondola and as a result, the system as a whole, in the interior of the tube, along with the changing pressure. This effect is significantly noticeable in various parts of the optical system such as the amplifiers, the microcontroller (PC104), the bottom part of the tube and the CCD camera. However, the performance of the Fabry-Perot and the filters was slightly affected by fluctuations in temperature, which is clearly represented in Fig. 5.1:

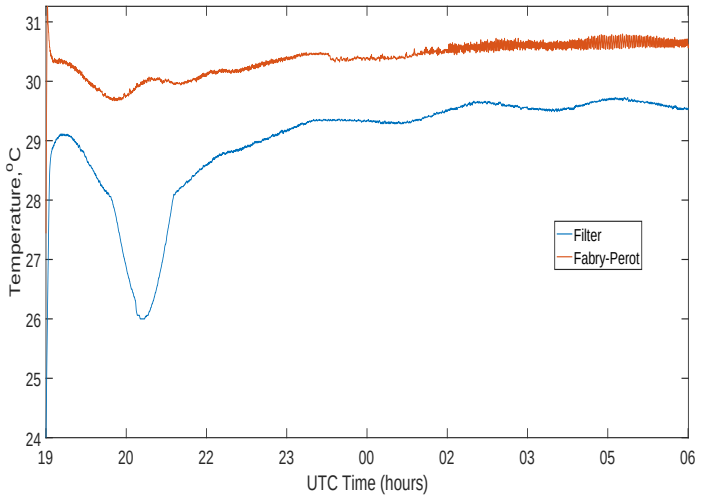

Fig. 5.1: Change in temperature for the entire duration of the balloon flight.

The graphs represent the F-P spectrometer and the interference filters. As seen from above, the temperature sensors that were placed on the surface of the spectrometer display a relatively stable temperature with small variations. Initially, the temperature is at its highest at 31.56°C, followed by a sudden drop and reaching a minimum of 27.44°C within the first hour. After the first half of the flight (≈01:00 UTC time) until descent there is very little change and the average temperature is ≈30.55°C. The interference filters, on the other hand, exhibit a larger temperature variation, especially during the first three hours, where the temperature drops to a minimum of 26°C at approximately 21:05 UTC time, gradually rises until a value of 29.32°C is reached and fluctuates around an average value of 29.6°C until the end of the flight.

A scan must be chosen where we have the least variation in temperature at the spectrometer and the filter surfaces throughout the total duration of the scan (10 minutes). For this reason, step scan 36 done at approximately 3:08 UTC will yield better results. The temperature of the filters remains at a constant value of $T_{filters}$=29.62°C, in contrary to the F-P, which shows a small fluctuation with an average value of $T_{F-P,mean}$=(30.7±0.15)°C.

The observed spectrum for scan 36 for pixels at the centre of the

detector (512, 512) and at normal incidence is shown in Fig. 5.2. The transmittance is plotted against wavelength and is not corrected for temperature change:

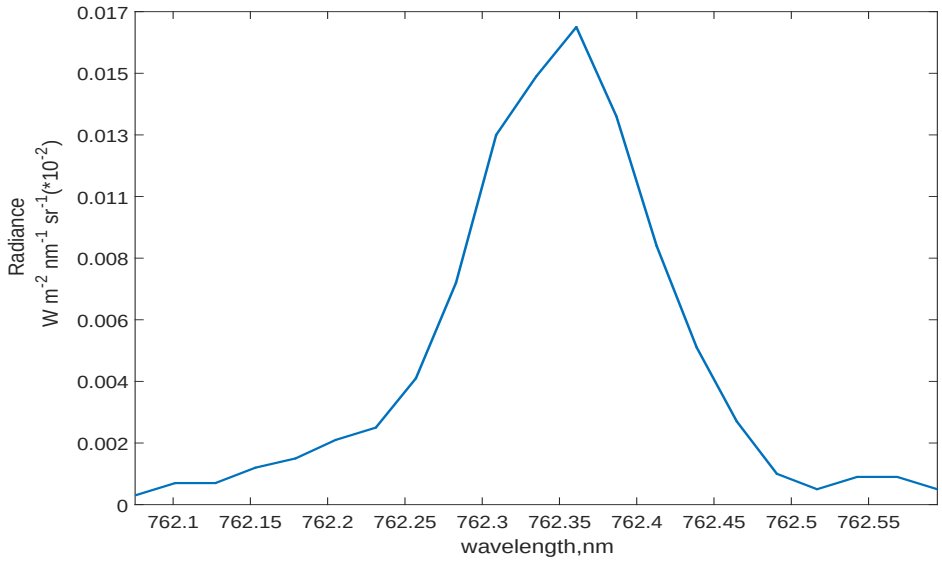

Fig. 5.2: The observed spectrum generated in Alice Springs from step scan 36.

A simulated spectrum representing the absorption lines in the O_2 band in the spectral range from 761.9 nm to 762.9 nm was provided by Chris Sioris. It was retrieved at a zenith angle of 33.9 degrees at York University on July 27, 2016. The spectrum was based on a VECTOR radiative transfer model (RTM) simulation that takes into account an optical depth of 0.05 and a

surface albedo of 0.18 for the viewing geometry. The model that was used is MODTRAN 5.2 and the line parameters are obtained from HITRAN 2008. The spectrum is shown in Fig. 5.3:

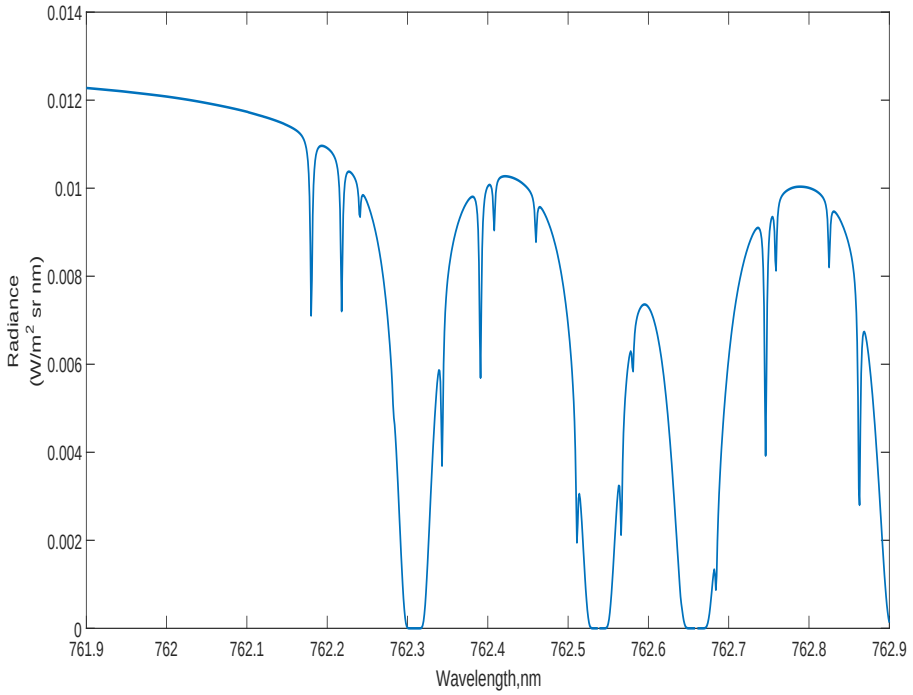

Fig. 5.3: Simulated spectrum of the O_2 absorption band. Courtesy of Dr. Chris Sioris.

The spectral radiance is in units of W m^{-2} sr^{-1} nm^{-1} and is plotted against the wavelength. Three major absorption features are noticeable in the figure at wavelengths 762.31 nm, 762.538 nm and 762.66 nm respectively.

Since the original objectives of the project require observations in the O_2 band at 762.31 nm, our measurements and calculations will focus on this spectral line. For this reason, the spectral range at which the Fabry-Perot and the filters operate are of major importance. Any temperature changes that could have altered their performance during the flight mission should be taken into account.

In section 3.2 the temperature coefficient of the filters was measured at α=0.0203 nm/°C and the operating temperature is T_{op}=23°C, as provided by the manufacturer. Since the temperature throughout scan 36 was $T_{filters}$=29.82°C the shift in wavelength will be $\Delta\lambda=\alpha(\ T_{filters}\text{-}T_{op})$=0.138 nm. As there are two almost identical filters inserted in the front optics tube of the instrument, the total transmission will decrease by 23%, as shown in Fig. 5.4, with a wavelength at maximum transmission of λ_o=762.4075 nm, at normal incidence. Therefore $\lambda\text{-}\lambda_o$=0.134 nm or λ=762.542 nm is the shifted center wavelength. The shape of the filter at both temperatures is shown in Fig. 5.4 :

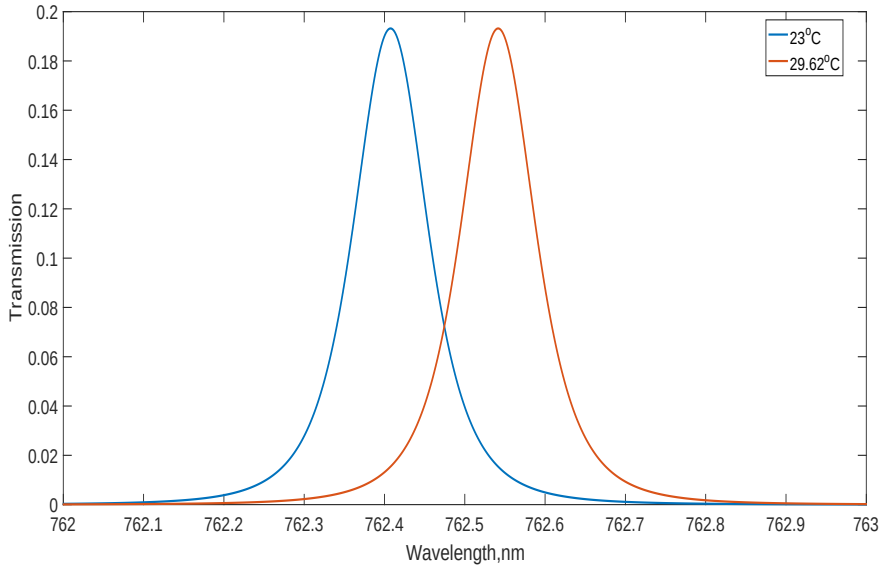

Fig. 5.4: Shift of filter wavelength with temperature change (δT=6.62^{o}C) during flight.

From Fig. 5.4 it is clear that the shift in wavelength results in reduced transmission of 0.26% for the first O_2 atmospheric band at 762.31 nm. This is an important issue, as sufficient spectral information cannot be obtained in this spectral band, due to low transmission. However, measurements can be carried out in the second absorption band of the spectrum at 762.538 nm, where the peak transmission is significantly higher. Since the filters peak (λ=762.545 nm) at a slightly different wavelength than the line spectra (λ_o=762.538 nm), increasing the angle of incidence through the instrument

and, therefore on the detector, by a certain amount will lower the centre wavelength of the filters in order to coincide with the absorption line. Using the formula from section 3 and rearranging we get :

$$sin\theta = \frac{n_{ef}}{n_o}\sqrt{1 - \frac{\lambda^2}{\lambda_o^2}} \tag{5.1}$$

which gives an angle of θ=0.523 degrees, with parameters n_{ef} and n_o defined from above. This half angle is subtended by an interference ring on the detector imaging area that has a radius of r=$f$tanθ=3.83 mm, given the focal length f=420 mm. This translates to a radial distance of d≈160 pixels, so all step scans that correspond to this radius are averaged and this is done for both the instrumental passband as well as the observed spectrum obtained from the flight.

In section 3.3 the effect the temperature has on the spectrum obtained from the step scans was determined, as well as the temperature coefficient of the spectrometer $\alpha_{F\text{-}P}$=0.0129 nm/°C. The results obtained with the temperature controller were selected as better data, rather than with the thermocouple as the tests were conducted in a more controlled procedure. The second peak of the step scan conducted in the laboratory at room temperature ($T_{op,F\text{-}P}$=24.5°C) occurs at 762.4 nm, so the wavelength shift, as was with the case of the filters, will be $\delta\lambda$=α(T-$T_{op,F\text{-}P}$)=0.0686 nm. The final

temperature is defined above as T=29.82 °C and the final peak wavelength becomes λ=762.469 nm. The figure below represents this change :

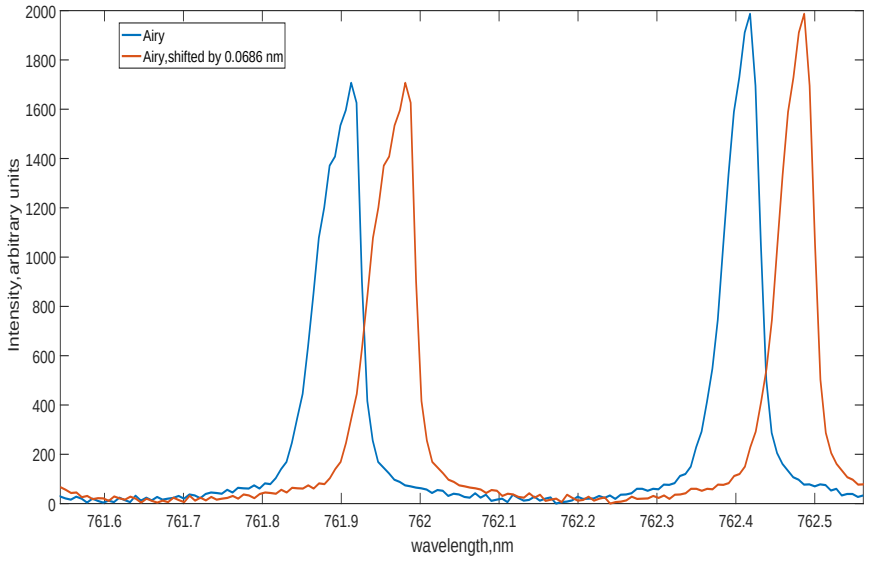

Fig. 5.5: Instrumental passband (Airy profile) retrieved at 24.5°C and at 29.82°C respectively.

The wavelength shift of the observed spectrum due to temperature change will be the same as the instrumental passband $\delta\lambda$=0.0686 nm, so at an angle of θ=0.523 degrees (160 pixels radial distance) the profile that is obtained is shown below in Fig. 5.6 :

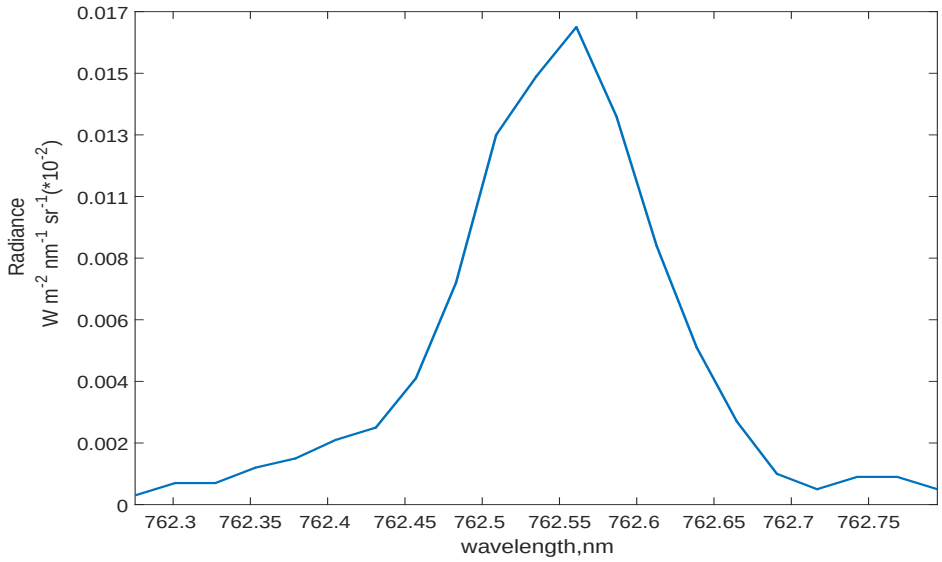

Fig. 5.6: The observed spectrum generated in Alice Springs from step scan 36 at θ=0.523 degrees and corrected for temperature change

The recorded profile function $Y(\sigma)$ represented in Fig. 5.6 can be considered to be a convolution of the instrumental profile $W(\sigma)$ with the true line spectrum $B(\sigma)$ [22]:

$$Y(\sigma) = W(\sigma) \star B(\sigma) \tag{5.2}$$

where σ=$1/\lambda$ denotes wavenumber and the instrumental profile $W(\sigma)$ has been determined in Fig. 5.5. Thus, the true atmospheric spectrum can theoretically be obtained through a deconvolution between $Y(\sigma)$ and $W(\sigma)$. This procedure however isn't straightforward and does not yield good results in

Matlab, so a different approach is used. The transmission values of the filter shape are divided with those of the observed profile, provided that the same spectral range is selected. In this way, an estimate of the true line profile is generated. The following figure shows the resulting spectrum:

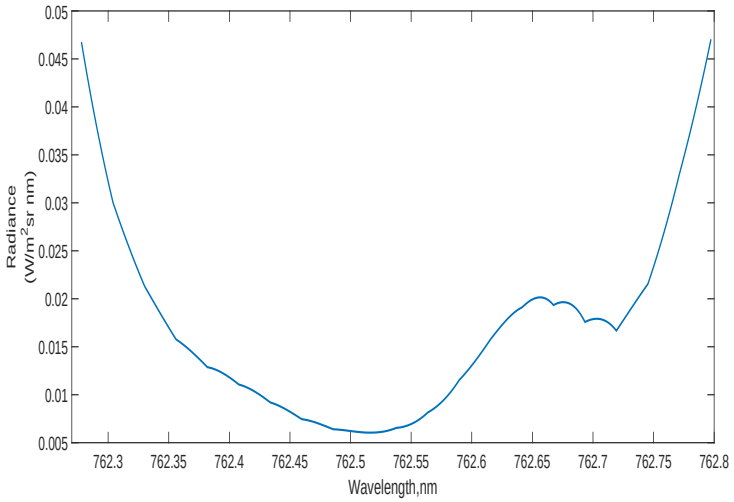

Fig. 5.7: The true spectrum generated from the recorded and filter profiles

The wavelength values on the x-axis of Fig. 5.7 possibly do not represent the true wavelengths present. This is due to the fact that constant temperature fluctuations during the flight mission might have altered the recorded spectrum. Also, the system optics may have encountered a wavelength shift due to a temperature of bigger magnitude than was measured in the lab. It is quite clear that the spectrum strongly resembles the O_2

absorption line at 762.66 nm, comparing it with the modelled atmospheric spectrum of Fig. 5.3.

To better visualize the behaviour of the O_2 spectra, as well as the filters and the instrumental passband, as shifted with temperature the transmission is plotted for all three in a single graph:

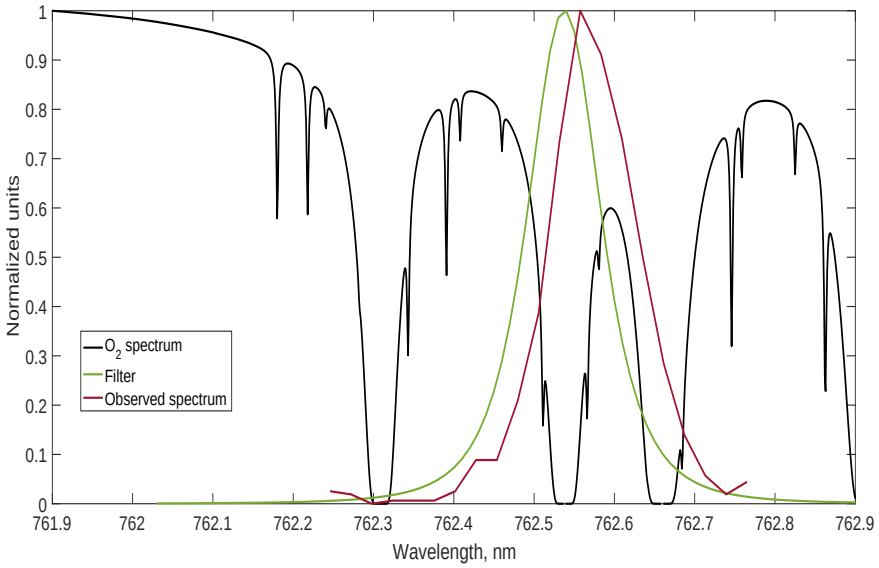

Fig. 5.8: O_2 atmospheric spectrum, filter and observed profile.

All the above three curves have been interpolated in wavelength scale with a small increment of $\delta\lambda$=0.0001 nm in order to represent them in one plot. Shift of wavelength with temperature (as measured in the lab) has been taken into account.

5.2 Variation of albedo during flight

The overall objective of the observations made in Section 5.1 was to interpret them in terms of physical quantities of the atmosphere as well as of the surface. The most important physical parameters that we are interested in are surface albedo, atmospheric thickness and the presence of light cloud. In this thesis only the first of these, the surface albedo is addressed and modelled. In order to proceed to the calculation of the albedo, a time series was generated that represents the variation in the observed radiance that reaches the detector throughout the duration of the flight. For this purpose, scans 15 through 50 were selected, where the exposure time was 30 seconds. For each of these step scans, the counts were averaged over a radial distance of 350 pixels from the centre of the fringes, which was calculated at (550, 380) on the CCD. This was done for each step so as to reduce the noise, and the maximum counts were observed, converted to actual radiance and plotted against the scan number as well as the UTC time as follows:

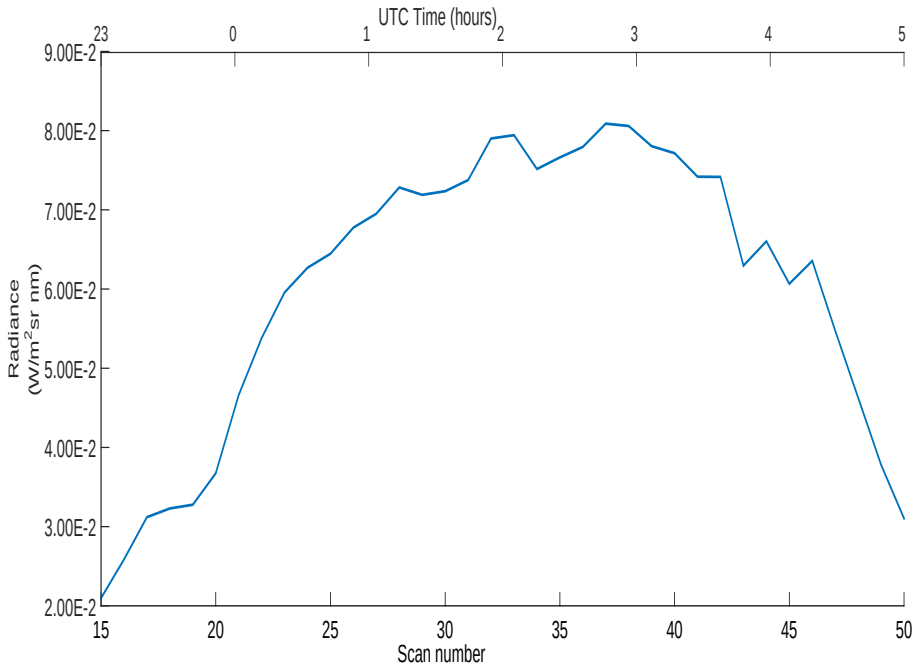

Fig. 5.9: Change in maximum observed radiance with time and scan number

The maximum radiance points on the scan as seen in Fig. 5.9 are taken as wavelength without O_2 absorption, and therefore surface absorption. The radially averaged step scans over the course of the flight, corresponding to scan15 until scan50 are shown below:

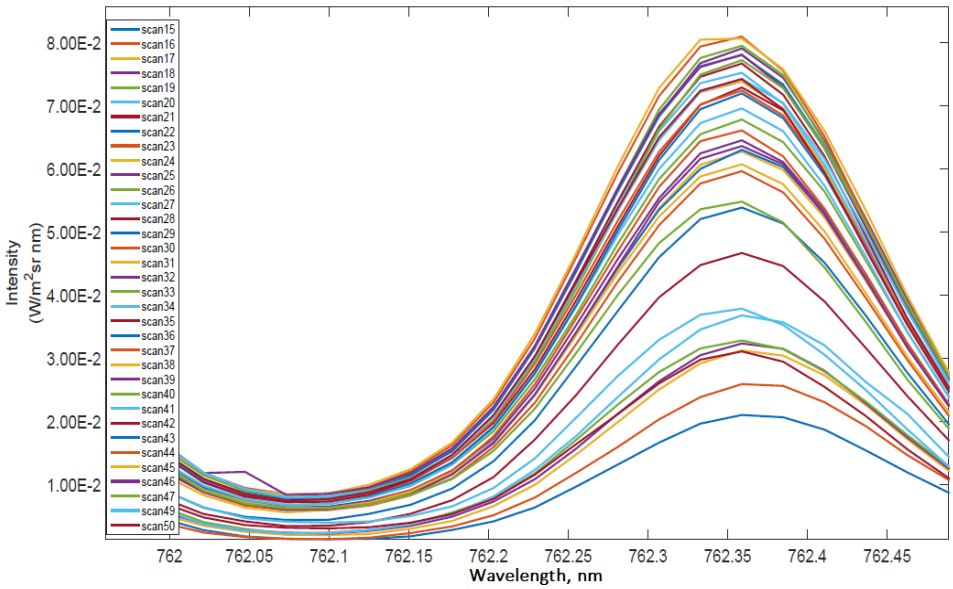

Fig. 5.10: Radially averaged step scans 15-50

The goal is to estimate the variation of the albedo during the flight until the last scan was performed. In order to proceed to the calculation of the albedo, the solar zenith angle must be found for each step scan, based on the GPS data provided by CNES (Centre National d'Etudes Spatiales) for the entire duration of the flight. The equation that is used for the zenith angle estimation is [24]:

$$\cos(\phi) = \sin(lat)\sin(decl) + \cos(lat)\cos(decl)\cos(ha) \tag{5.3}$$

where lat is the latitude, dec is the solar declination and ha the hour angle. The change of the angle with time is shown below:

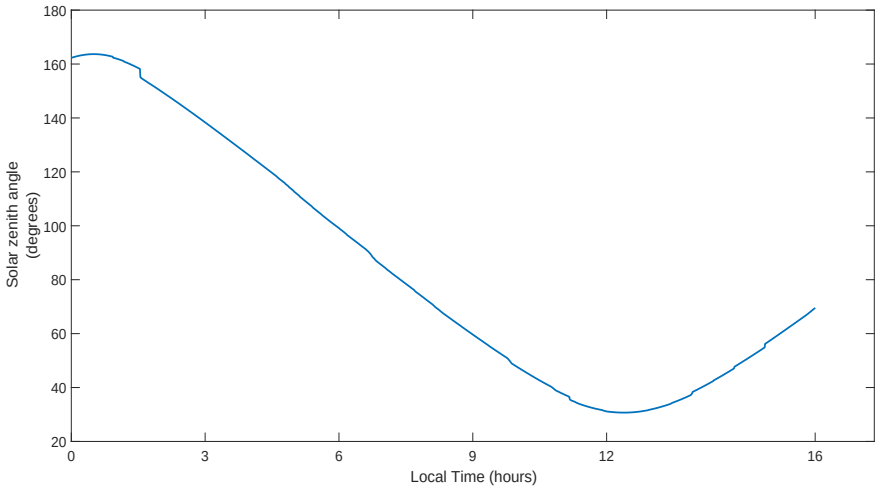

Fig. 5.11: Solar zenith angle as a function of time (Alice Springs local time)

From Fig. 5.11 we clearly notice a continuous change of the solar zenith angle throughout each scan, and consequently throughout the flight. An effective way should therefore be found so as to remove the dependence of the albedo on the zenith angle value. To do this, a theoretical model is taken into account that was provided by Dr. Sioris and represents a time series of radiance at a wavelength of 762.13 nm over a barren desert. The surface albedo, which is the most appropriate for Alice Springs, in this case is assumed to be ≈0.36 at 760 nm. The spectral resolution of the simulation is based on a Finesse of 3.83, with background aerosols taken into account. The model is strongly dependent on the altitude variation of the balloon,

with an assumed surface elevation of 563 m above sea level, based on the GPS altitude data before launch, as provided by CNES. The time series is shown below:

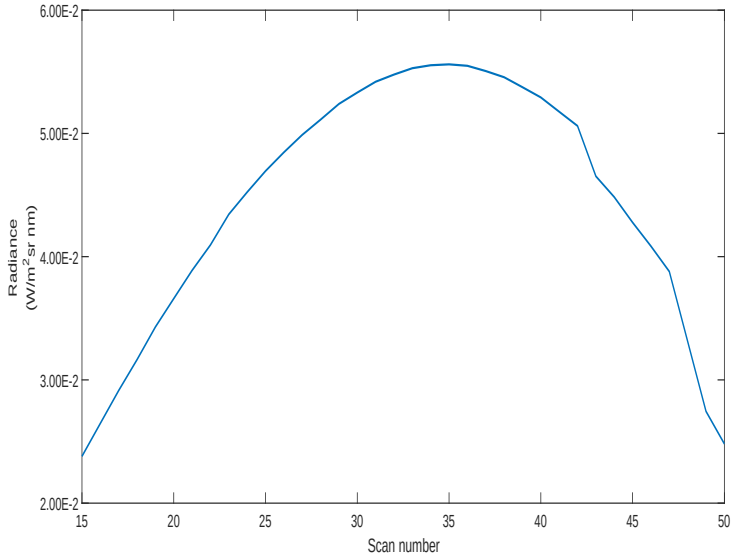

Fig. 5.12: Variation in observed radiance as a function of scan number. Courtesy of Dr. Chris Sioris.

Since the radiance values correspond to scans 15-50, an initial albedo of 0.36 that was mentioned previously is assumed for scan15, so that the scene albedo α_i for all subsequent scans can be obtained by:

$$\alpha_i = 0.36 \frac{(R_{measured,i}/R_{measured,15})}{(R_{modelled,i}/R_{modelled,15})} \tag{5.4}$$

where $R_{measured,i}/R_{measured,15}$ is the ratio of the measured radiance for each

scan number i to the radiance obtained for scan15 that was generated from Fig. 5.9 and $R_{modelled,i}/R_{modelled,15}$ the ratio of the radiances provided in Fig. 5.12 by Dr. Sioris' simulation. In this way, the solar zenith angle dependence of the measured radiance values is successfully removed and the variation in the albedo, based on Eq. (5.4) is shown in the following figure:

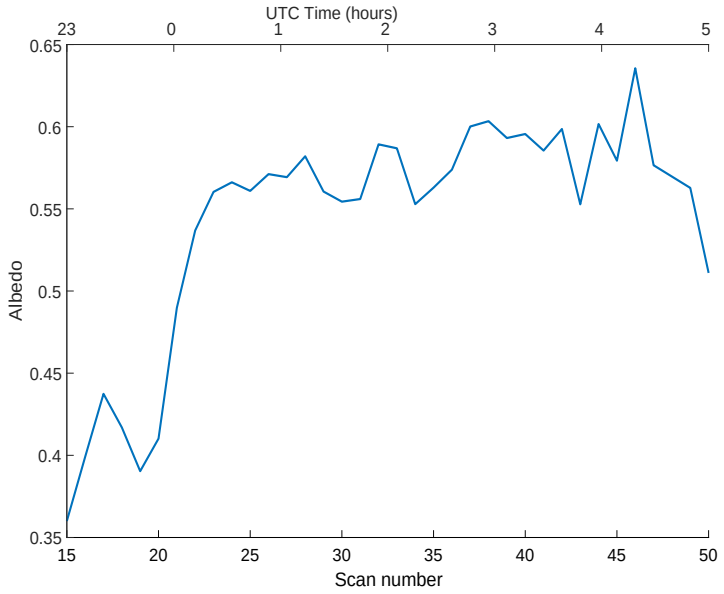

Fig. 5.13: Change of albedo as a function of scan number, after the removal of the solar zenith angle dependence.

Chapter 6

Conclusions and future work

The primary objective of the research involved in this thesis was to characterize and test the performance of the Fabry-Perot spectrometer, as part of an optical assembly. Apart from this, atmospheric data analysis obtained from the flight was also performed, mainly regarding O_2 absorption measurements and albedo variation. The calibration tests that were carried out in the lab will give us insight on any implications involved when integrating this spectrometer into an instrument that has to meet certain scientific criteria. The range of values of the reflectivity Finesse was estimated to be close to the desired value ($\sim$30), at the time when SDCNLAB had received the Fabry-Perot from MPBc. However, the tests described in section 3.4

that were done by placing an aperture in different positions relative to the etalon showed that the Finesse varied as one moves across the etalon, as well as for off-axis angles. This was possibly due to errors related to parallelism between the two mirror flats of the Fabry-Perot.

Using a different optical setup, a variation of gap spacing was measured across the surface of the etalon, which also revealed imperfections associated with the Fabry-Perot. For this reason, the instrument was shipped back to MPBc in order to apply a mask that would isolate the portion of the etalon that experienced the least variation and had a uniform gap spacing. However, tests that were done on the improved version of the spectrometer revealed a low Finesse value in the range 9.5-10. This should be taken into account and the reasons that lead to this significant change should be studied for future research projects to be carried out.

The response of the Fabry-Perot to temperature change was measured with two methods: By using a thermocouple and with the use of a Minco temperature controller. The temperature coefficients that were obtained with both methods were 0.0206 nm/°C and 0.0129 nm/°C respectively. The second method that involved the temperature controller seems to be a more accurate method to estimate the wavelength change, as the thermofoil heaters

were only attached to the Fabry-Perot. Whereas in the first method the heat was distributed into the entire closed system and more time was required for the temperature to stabilize in order to take measurements. However, due to low thermal conductivity, the filter may be at a different temperature than the heaters are controlled at. The local heating of the etalon might therefore not be very applicable to obtain data. Errors associated with the temperature readings were also present in both methods, as the temperature was constantly changing over the course of the measurements. Other possible ways that yield results of higher accuracy should be looked into in order to better understand the performance of the spectrometer when high temperatures are present.

Tests that were done on the O_2 interference filters used in the flight gave a temperature coefficient of 0.0203 nm/°C, which is in agreement with the value provided by Andover. Although the diffraction grating spectrometer proved to be an accurate way of measuring wavelength change with temperature, experimental errors and challenges were present when measuring the filter passband. More attention should be paid to the alignment of the entrance optics, as possible misalignment between the filters and the source can make a significant impact on the results. Also, there is a no-

ticeable amount of background noise as we can clearly see in Fig. 4.17 that represents the filter shape. This is mainly due to the fact that the etendue or the f/number of the entrance optics should be smaller than that of the monochromator (Czerny/Turner monochromator in our case) and any deviation will contribute to unwanted stray light. Therefore, the size of the aperture stop must be chosen wisely in order to fill the diffraction grating perfectly.

Finally, the spectrum that was generated from the observed profile and filter passband based on the flight data, apparently represents the absorption feature of the O_2 line at 762.66 nm. This is different from what was expected for the 762.53 nm feature, which might be due to a larger wavelength shift of the F-P due to temperature ($\sim$29.6 °C) when the system was at float.

Nevertheless, it was possible to make use of the wavelength variation with off-axis angle to obtain acceptable spectra for this different line. Obtaining atmospheric parameters from the spectrum may be possible but will require considerable additional work. Improving the finesse in future would allow the desired resolution to be obtained, and make it possible to cover a larger spectral range. Absolute values of albedo were not obtained as the responsivity calibration was not consistent with the observed radiance from

the ground so while the variations presented are reasonable they are based on a simulated reference. The instrument itself worked extremely well and with the knowledge gained offers promise of excellent results in the future.

Bibliography

[1] Min, Q., Yin, B., Li, S., Berndt, J., Harrison, L., Joseph, E., Duan, M., and Kiedron, P., "A high-resolution oxygen A-band spectrometer (HABS) and its radiation closure," *Atmospheric Measurement Techniques*, Vol. 7, 2014, pp. 1711-1722.

[2] Mauderly, J. L. and Chow, J. C., "Health Effects of Organic Aerosols," *Inhalation Toxicology*, Vol. 20, No. 3, 2008, pp. 257-288.

[3] Hecht, E., *Optics*, Addison-Wesley, Reading, MA, 1998.

[4] Antonacci, G., De Panfilis, S., Di Domenico, G., DelRe, E., and Ruocco, G., "Breaking the Contrast Limit in Single-Pass Fabry-Perot Spectrometers," *Physical Review Applied*, Vol. 6, No. 5, 2016, pp. 4020.

[5] Betzler, Kalus., *Fabry-Perot Interferometer*, University of Osnabruck, 2002.

[6] Sanchez-Soto, L. L., Monzon, J. J., and Leuchs, G., "The many facets of the Fabry-Perot," *European Journal of Physics*, Vol.37, No. 6, 2016, pp. 064001.

[7] Tolansky, S., *An introduction to interferometry*, Longmans, London, 1955.

[8] Ebermann, M., Hiller, K., Kurth, S., and Neumann, N., "Design, Operation and Performance of a Fabry-Perot-Based MWIR Microspectrometer," *Proceedings OPTO*, 2009, pp. 233 - 238.

[9] Shepherd, G. G., Lake, C. W., Miiller, J. R., and Cogger, L. L., "A spatial spectral scanning technique for the Fabry-Perot spectrometer," *Applied Optics*,Vol. 4, No. 3, 1965, pp. 272.

[10] Moon, J. and Shkel, A. M., "Analysis of imperfections in a micromachined tunable-cavity interferometer," *Proceedings of the SPIE*, Vol. 4334, 2001, pp. 46-53.

[11] Shepherd, G. G., *Spectral Imaging of the atmosphere*, Elsevier Science, London, 2002.

[12] Anderson, O. L. and Schreiber, E., "The relationship between refractive

index and density of minerals related to the Earth's Mantle," *Journal of Geophysical Research*, Vol. 70, No. 6, 1965, pp. 1463-1471.

[13] Lerner, J. M., "Imaging Spectrometer Fundamentals for Researchers in the Biosciences-A Tutorial," *International Society for Analytical Cytology*, Vol. 69A, No. 8, 2006, pp. 712-734.

[14] Luhs, W., *Fabry Perot Resonator*, 2003.

[15] Lissberger, P. H., "Effective refractive index as a criterion of performance of interference filters," *Journal of the Optical Society of America*, Vol. 58, No. 12, 1968, pp. 1586.

[16] Smith, W. J., *Modern optical engineering*, McGraw-Hill, New York, 2000.

[17] Yeh, P., *Optical Waves in Layered Media,*, Wiley, N.Y, 1988.

[18] Shafer, A. B., Megill, L. R., and Droppleman, L., "Optimization of the Czerny-Turner Spectrometer," *Journal of the Optical Society of America*, Vol. 54, No. 7, 1964, pp. 879-887.

[19] Loewen, E. and Palmer, C., *Diffraction grating handbook*, Newport Corporation, Rochester, N.Y, 2014.

[20] Sigernes, F., Holmes, J. M., Chernouss, S., Svenoe, T., Dyrland, M., Lorentzen, D. A., Moen, J., and Deehr, C. S., *Sensitivity calibration of narrow field of view optical instruments*, The University Center in Svalbard (UNIS), 2007.

[21] Turgeon, E. C. and Shepherd, G. G., "Upper atmospheric temperatures from Doppler line widths," *Planetary and Space Science*, Vol. 9, No. 6, 1962, pp. 295-304.

[22] Hartmann, D. L., *Global Physical Climatology*, Academic Press, San Diego, CA, 1994.